Finite Element Analysis of Ductile Fracture Behaviour

of Pipe Sections with Surface Crack

Lutz Zybell

March 2005

Abstract

The goal of this project has been to study ductile fracture behavior of pipe sections with surface crack. We have successfully implemented the Gurson routine for 3D pipe models with "canoe" shaped surface crack in ABAQUS Explicit software. Furthermore, we have examined the influence of the dynamic simulation procedure on the trueness and accuracy of the results.

Concerning the ductile fracture behaviour of pipes with initial surface crack, we have found that for the specified model assumptions a decrease in load carrying capacity does not occur before the crack extended through all the wall thickness. Moreover, extensive determination of the Gurson parameters has shown that their variation only affects the point in time and load respectively when ductile tearing starts but not the ductile fracture behaviour itself. As regards final pipe failure it has been found that a different initial crack length results in different strain levels whereas the maximum load is indifferent to the initial crack length. Finally, we have ascertained that the crack growth resistance of pipes only depends on the initial crack length as long as this is less than 10 % of the circumference.

Acknowledgements

Task Description

Failure and leakage of underwater gas and oil pipelines is an important industrial concern and will result in dramatic consequence and economic losses. Understanding the fracture behaviour of pipelines will contribute to increasing safety and structural integrity of the pipe transportation system.

The aim of this student project is to study the ductile fracture behaviour of pipe sections with surface cracks by using the Gurson model implemented in ABAQUS Explicit software. 3D models with surface crack in a plate model will be created by PATRAN. The plate model will then be transferred to a real pipe model. Large deformation analysis should be used and the following parameters should be considered:

- Wall thickness: $t = 20\ mm$

- Ratio between outer diameter and wall thickness: $D/t = 20$

The fracture behaviour for that geometric parameters should be studied by adjusting the parameters in the Gurson routine to address the expected scatter in crack growth resistance found in offshore pipelines. The exact material data will be decided in collaboration with SINTEF.

The final report should include an introduction, modelling details, results and discussions. The results should be presented as deformation or load versus the crack tip driving forces (J or CTOD).

Prof. Zhiliang Zhang

Contents

List of Figures

List of Tables

Notation

Latin symbol	Meaning	Unit
a	Crack depth	mm
Δa	Crack growth	mm
c	Initial crack length	mm
c_d	Wave speed	$\frac{\text{mm}}{\text{s}}$
D	Outer pipe diameter	mm
d	Inner pipe diameter	mm
D_{el}	Elasticity tensor	-
E	Young's modulus	$\frac{\text{N}}{\text{mm}^2}$
f	Void volume fraction	-
f_0	Initial void volume fraction	-
f_c	Critical void volume fraction	-
f_F	Void volume fraction of final fracture	-
f_u^*	Void volume fraction of final fracture (Needleman/Tvergaard)	-
f^*	Void volume fraction (Needleman/Tvergaard)	-
g	Factor for calculating the time period	-
h	Width of the tearing zone	mm
J	J-Integral	$\frac{\text{mJ}}{\text{mm}^2}$
L	Length of the model	mm
L_e	Element's length	mm
l	Element's length	mm
l_x	Element's length in x-direction	mm
l_y	Element's length in y-direction	mm
$M1$	Path in Model 1	-
$M2$	Path in Model 2	-
m	Number of counted elements	-
n	Hardening exponent	-
q	Von-Mises effective stress	$\frac{\text{N}}{\text{mm}^2}$
q_1	First Tvergaard parameter	-
q_2	Second Tvergaard parameter	-
q_3	Third Tvergaard parameter	-
p	Hydrostatic stress	$\frac{\text{N}}{\text{mm}^2}$

Latin symbol	Meaning	Unit
r	Cylindrical coordinate (in System II)	mm
r_0	Initial relative density	-
s	Scaling factor for crack growth	-
T	Time period of simulation	s
T_1	Crack growth initiation	-
T_2	Reaching through crack	-
T_3	Final pipe failure	-
T^*	Time period for stress wave calculation	s
t	Wall thickness of plate resp. pipe	mm
Δt	Minimum stable time increment	s
Δt_{stable}	Stable time increment	s
U	Circumference of the pipe	mm
u	Special 1-coordinate (transformation in system III)	mm
V_{matrix}	Volume of the whole body	mm^3
V_{void}	Volume of the voids	mm^3
v	Special 2-coordinate (transformation in system III)	mm
W	Width of the modelled plate	mm
w	Special 3-coordinate (transformation in system III)	mm
x	Global 1-coordinate (in system I)	mm
y	Global 2-coordinate (in system I)	mm
z	Global 3-coordinate (in system I)	mm

Greek symbol	Meaning	Unit
Δ	Global displacement	mm
δ	Crack tip opening displacement	mm
ϵ	Strain	-
ϵ_{el}	Elastic strain	-
ϵ_{pl}	Plastic strain	-
Φ	Gurson yield function	-
ϕ	Cylindrical coordinate (in system II)	-
ν	Poisson's ratio	-
ρ	Density	$\frac{\text{t}}{\text{mm}^3}$
σ	Stress	$\frac{\text{N}}{\text{mm}^2}$
σ_y	Yield stress	$\frac{\text{N}}{\text{mm}^2}$
τ	Time	s
τ_1	Point in time for crack growth initiation	s
τ_2	Point in time for reaching through crack	s
τ_3	Point in time for final pipe failure	s

1 Introduction

In this project, ductile fracture behaviour of surface cracked pipes was analysed using the finite element method (FEM). Pipe fracture is an important industrial concern in Norway. Prior to this study ductile fracture behaviour was successfully simulated at SINTEF[1] for 2D structures by implementing the Gurson model in ABAQUS Standard software. However, all 3D simulations failed due to convergence problems. Thus the main aim of this project was simulating ductile fracture behaviour for 3D pipe models in ABAQUS Explicit software.

A FE simulation procedure consists of the following steps: At first a FE model must be created by defining the geometric and physical data. We used the FE programme PATRAN to create the input files containing the geometric data. All physics were later added to the input files in the text editor vGim. After on the analysis based on the input files were run in ABAQUS Explicit software before we finally analysed the results in ABAQUS Viewer. The whole simulation process is depicted in Figure 1.1:

Simulation Process

Pre-processing → Analysing → Post-processing

PATRAN / gVim   ABAQUS   ABAQUS Viewer

Pre-processing

To create a FE model by defining:

- Geometry
- Mesh
- Material
- Load
- Analysis procedure
- Output
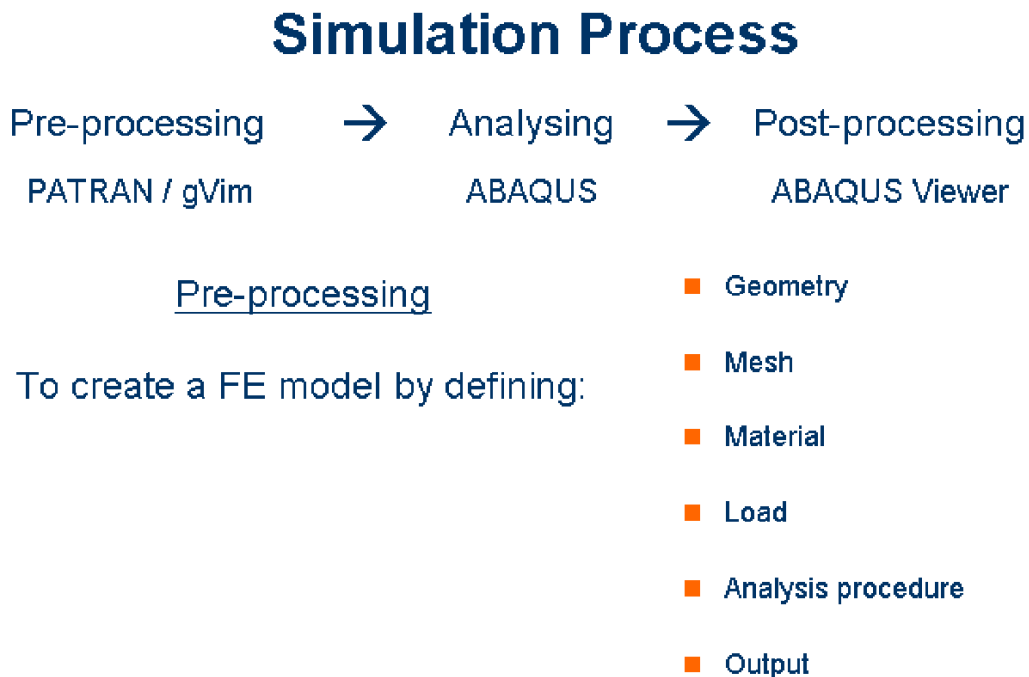
Figure 1.1: Simulation process

---

[1]SINTEF means The Foundation for Scientific and Industrial Research at the Norwegian Institute of Technology (NTH).

Simulations done at SINTEF prior to this study have greatly influenced the methods and the definition of parameters used in this work. Thus, in this project the priority was given to the tensile load case. The common modelling strategy of creating a surface cracked plate and afterwards transferring it into a pipe was realised. Moreover, ductile material behaviour was implemented and further investigation on the influence of parameters concerning procedure and geometry was conducted in order to achieve better understanding of ductile fracture behaviour of pipe sections with surface crack.

2   Theoretical Background

2.1   Elastic-plastic Fracture Mechanics

Medium strength steel, which has a typical elastic–plastic fracture behaviour, is usually used for oil pipelines. Consequently, elastic–plastic fracture mechanics is applied in this project bacause plastic material deformation does not only occur in a very small region near the crack tip. To describe the crack opening behaviour of elastic–plastic material, the crack tip opening displacement (CTOD) is commonly used as a failure criterion. This parameter is described in Section 2.1.1 and in Section 2.1.2 the basics of crack growth resistance are explained.

2.1.1   Crack Tip Opening Displacement

The crack tip opening displacement δ was introduced by Wells in the 1960's. He discovered that crack faces of medium-strength structural steels moved apart with significant plastic deformation. As these materials were too ductile to be characterized by linear elastic fracture mechanics, Wells proposed CTOD as an alternative failure criterion.
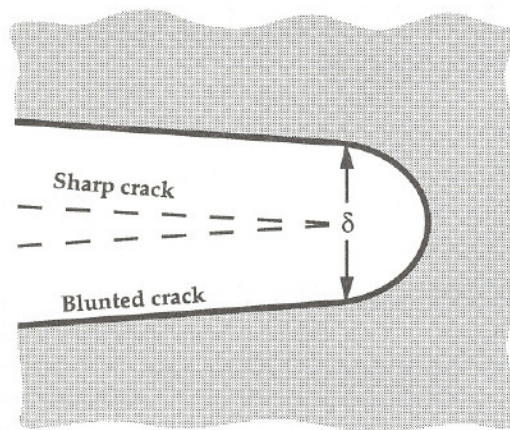
Figure 2.1: Crack tip opening displacement [1]

CTOD is measured according to Figure 2.1, which shows that an initially sharp crack has blunted due to plastic deformation. Simultaneously the degree of blunting increases in proportion to the toughness of the surrounding material. Therefore Wells proposed the value of CTOD δ as a measure of fracture toughness [1].

2.1.2   Crack Growth Resistance Curves

Crack growth resistance curves are commonly plotted as J-integral versus crack extension Δa, where J is another failure criterion parameter in elastic-plastic fracture mechanics. Since the output for the J-integral is not available in ABAQUS Explicit the graphs for crack growth resistance in this

report display the behaviour of CTOD δ versus crack growth Δa. Using J, a rising CTOD curve, in metals is naturally associated with growth and coalescence of micro voids (see Section 2.2.2), should be expected.

2.2   Ductile Fracture

Ductile fracture is one of the most common fracture mechanisms in metals, where ductile materials fail as a result of nucleation, growth and coalescence of micro voids. Figure 2.2 displays the whole ductile fracture process. The single steps are explained in the following subsections.
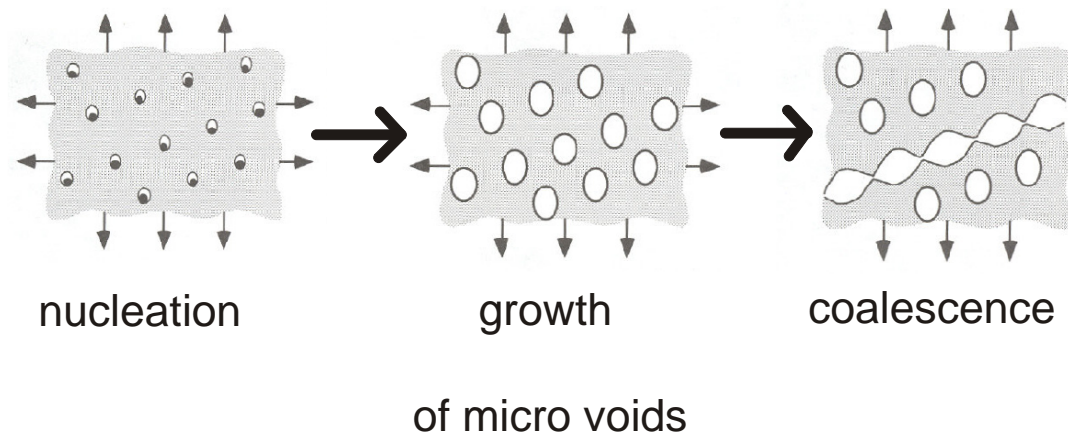
Figure 2.2: Ductile fracture process (based on Anderson [1])

2.2.1   Void Nucleation

Voids nucleate at inclusions or second phase particles when enough stress is applied. Then the interfacial connection between particle and matrix is broken. The nucleation of the void is often the critical step and fracture happens soon after that. However, for materials, where the voids nucleate easily, the fracture behaviour is controlled by void growth and void coalescence [1].

2.2.2   Void Growth and Coalescence

Void growth is caused by increasing plastic strain and hydrostatic stress after void nucleation. For a relative low initial void volume fraction f, what is described in Section 2.2.3, the void growth goes off independently. But after f becomes larger than a certain critical value f_c neighbouring voids will interact. Plastic strain is concentrated along several voids and local necking starts. This and continuing void growth finally lead to connection of the voids what is equal to separation of material [1] [7].

2.2.3   The Gurson Model

In 1977, Gurson found a mathematical function, that partly describes part of ductile material behaviour. He proposed a yield condition as a function of the void volume fraction f for a metal containing a dilute concentration of voids [5]. In this condition the void volume fraction f is the ratio between the volume of voids V_{void} and the volume of the whole matrix V_{matrix}:

$$f = \frac{V_{void}}{V_{matrix}} \tag{1}$$

Gurson's yield condition bases on the spherically symmetric deformation of a rigid-perfectly plastic body around a single spherical void and can be written in the following form, where q denotes the von-Mises effective stress, σ_y represents the yield stress and p is the hydrostatic stress:

$$\Phi = \left(\frac{q}{\sigma_y} \right) + 2 f \cosh \left\{ - \frac{3}{2} \frac{p}{\sigma_y} \right\} - \left(1 + f^2 \right) = 0 \tag{2}$$

In 1981, this yield condition was modified by Tvergaard. He introduced the parameters q_1, q_2 and q_3 (where $q_3 = q_1^2$) as constant coefficients of the void volume fraction and the pressure terms. The aim was to make the predictions of the original Gurson model more exact. The original Gurson model can be recovered by setting $q_1 = q_2 = q_3 = 1$ [6]:

$$\Phi = \left(\frac{q}{\sigma_y} \right) + 2 q_1 f \cosh \left\{ - \frac{3}{2} \frac{q_2 p}{\sigma_y} \right\} - \left(1 + q_3 f^2 \right) = 0 \tag{3}$$

However, this modified Gurson model just describes void growth; thus a simulation of void coalescence was still missing. In 1984, Needleman and Tvergaard defined Equation 4 in order to simulate void coalescence, where f in Equation 3 must be replaced by f^*. Furthermore in the following equation f_u^* is calculated by $f_u^* = 1/q_1$, while f_c represents the critical void volume fraction and f_F is the void volume fraction of final failure:

$$f^* = \begin{cases} f & \text{for } f \leq f_c \\ f_c + \frac{f_u^* - f_c}{f_F - f_c} + (f - f_c) & \text{for } f > f_c \end{cases} \tag{4}$$

This function implies that after void coalescence has started ($f > f_c$), the void volume fraction is amplified as displayed in Figure 2.3. Before void coalescence ($f \leq f_c$) the void growth and the decrease of load carrying capacity follows the modified Gurson model according to Equation 3.

2.3   Implementing Ductile Material Behaviour in ABAQUS

Simulating ductile material behaviour therefore consists of two steps. At first, a basic elastic–plastic material behaviour must be defined, what is further described in Section 2.3.1, before the Gurson model can be implemented according to Section 2.3.2.
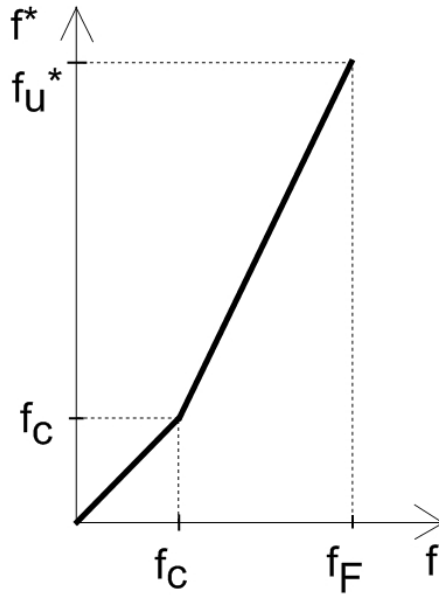
Figure 2.3: Void coalescence described by Equation 4

2.3.1   Defining Elastic-plastic Material Behavior

In ABAQUS elastic material behavior is determined by the *ELASTIC option. Young's modulus E and Poisson's ratio ν have to be specified by the user. The total stress σ is defined from the total elastic strain ϵ_{el} as

$$\sigma = D_{el} \, \epsilon_{el} \tag{5}$$

where D_{el} is the fourth-order elasticity tensor. This equation can be simplified for the uniaxial case and results in Hooke's law:

$$\sigma = E \, \epsilon_{el} \tag{6}$$

This linear elastic model only works for small elastic strains (less than 5 %) until parts of the model reach the yield stress. Near the cracktip plastic deformation will occur for sure. Thus plastic behaviour is described by implementing isotropic hardening based on the von-Mises yield surface. Using ABAQUS yielding is defined by giving the value of flow stress σ (for $\sigma > \sigma_y$) as a function of equivalent plastic strain ϵ_{pl} on the data lines of the *PLASTIC option. This data, added to the input file, can be previously calculated by the user according to the following power law:

$$\sigma = \sigma_y \left(\frac{\epsilon_{pl} \, E}{\sigma_y} + 1 \right)^n \tag{7}$$

In Equation 7 σ_y is the yield stress and n represents the strain hardening exponent. This power law is usually used at SINTEF to assume material with rate-independent strain hardening [8].

2.3.2 Implementing the Gurson Model in ABAQUS

The Gurson model is implemented in ABAQUS with the *POROUS METAL PLASTICITY option. That means that the Gurson yield function (Equation 3 from Section 2.2.3) is used to calculate the void volume fraction f. The Tvergaard parameters must be defined by the user. $q_1 = 1.5$, $q_2 = 1.0$ and $q_3 = q_1^2 = 2.25$ are reported in [3] as typical ranges of the parameters. In addition, the initial relative density r_0 of the material is defined as:

$$r_0 = 1 - f_0 \tag{8}$$

It has to be added to the data line of the *POROUS METAL PLASTICITY option in the input file. r_0 is inversely defined to the initial void volume fraction f_0 as the ratio of the solid material (without voids) to the total volume of the material.

Void coalescence and final failure of the elements are only possible to model in ABAQUS Explicit with the *POROUS FAILURE CRITERIA option. The Needleman/Tvergaard function (Equation 4 from Section 2.2.3) is used to simulate void coalescence after reaching the critical void volume fraction f_c. Both failure criterion parameters, f_c and the void volume fraction of final failure f_F, have to be defined by the user as well.

Since $f_F = 0.15 + 2\,f_0$ is proposed in [7] as an approximate equation for final failure. According to Zhang [2], $f_c \approx 0.03$ is a more realistic value to characterize critical void volume fraction than former used greater values. The input data for the failure criterion was defined as shown in Table 2.1 in order to reach a curve shape of the void coalescence criterion like in Figure 2.3 in Section 2.2.3 displayed:

r_0	f_0	f_c	f_F
$[-]$	$[-]$	$[-]$	$[-]$
0.995	0.005	0.03	0.16

Table 2.1: Overview of failure criterion parameters

Due to comparability with former simulations at SINTEF in this project the *VOID NUCLEA-TION option in ABAQUS was not used and all initial voids were defined by the initial relative density r_0 without any additional void nucleation.

2.4 Processing in ABAQUS Explicit

Since we have used ABAQUS Explicit software in this project, this section gives an overview over the important features of the explicit calculation method.

The difference between ABAQUS Standard and ABAQUS Explicit lies in the calculation method, especially in gaining the accelerations of the nodes. In the implicit method the global tangent stiff-

ness matrix and as well iterations and tolerances are required, which are expensive in calculation time and can lead to numerical difficulties.

2.4.1 Finite Element Method in Explicit Dynamics

In ABAQUS Explicit the calculation method is, as the name implies, strongly explicit. The state at the end of an increment is solely based on the displacements, velocities and accelerations at the beginning of that increment in time. The calculation during that increment increment processes as follows:

Dynamic equilibrium is established for each node at the beginning of an increment. The acceleration of the nodes is only calculated by its mass and the net force (difference between external applied forces and internal nodal forces) acting on it. Thus, these calculations are cost–efficient. By time integration based on a central difference rule the established equations of motion are explicitly integrated through time and obtain the nodes' velocities and displacements. Then the strain increments of the element and finally its stresses are calculated from the nodes' velocities. As the last step, the internal forces of the nodes are reset before the dynamic equilibrium at the beginning of the next increment can be solved [3].

2.4.2 Stability Limit

To produce accurate results the time increments for integration must be very small. The stability limit Δt_{stable} for producing still reliable and accurate results is given by the following estimation (according to the ABAQUS Manual [3]):

$$\Delta t_{stable} = \frac{L_e}{c_d} \tag{9}$$

where L_e is the smallest element length and c_d is the wave speed of the material. The wave speed c_d is only a material property and can be calculated by extracting the square root of the quotient of Young's modulus E divided by the mass density ρ:

$$c_d = \sqrt{\frac{E}{\rho}} \tag{10}$$

Equation 9 and 10 show that the higher the density, the lower the wave speed, which finally results in a larger stability limit. Thus fewer increments are needed to run through all the process time period T and the time of computation will be less.

2.4.3 Quasi-static Analysis

Although the explicit solution method was originally developed to model dynamic events, it can also solve static problems. When models become very large, the explicit procedure requires less

computer resources than the implicit one.

Applying ABAQUS Explicit to quasi-static problems first of all requires special consideration about the time period T of the event. The safest way, of course, would be using the actual time, which the physical process takes in nature. But the process can also be modelled using a shorter time period T, still producing the same results.

The following example explains the influence of load rating:

If load is applied e.g. on one end of a tensile bar too fast (whereas a high load rate is equal to a short time period T of the process), only the elements on that end will be influenced and distorted. But the goal of quasi-static modelling of a process is that all elements along the bar's length should be uniquely distorted.

Hence, an appropriate time period T of the process must be chosen. It can be defined by calculating the time T^*, which a stresswave needs to travel through the length L of the model once, and multiply it by a factor of $g \geq = 10$. The estimation, which is displayed in Equation 11, is commonly used at SINTEF for dynamic modelling [10].

$$T = g \, T^* = g \, \frac{L}{c_d} = g \, L \, \sqrt{\frac{\rho}{E}} \tag{11}$$

The second point of attention is the application of loading. In order to achieve accurate results of quasi-static analyses the load must be applied as smooth as possible. By the automatic built-in SMOOTH STEP type of the *AMPLITUDE option in ABAQUS the applied changes in acceleration are as small as possible. So the changes in velocities and of course displacements will also be smooth. In order to assure that the quasi–static simulation produces reasonable results, various model energies should be studied. The following propositions can be established according to the ABAQUS Manual[3] as general rules for quasi–static simulations and have to to be prooved:

- The kinetic energy of the model should not exceed 5 % of the internal energy.

- The work applied by external forces should be almost the internal energy of the model.

2.4.4   Mass Scaling

In order to obtain an economical solution for simulations with a large number of small elements, the calculation time must be shortened in some way. There are two possibilities, namely load rate scaling and mass scaling. Since load rate scaling is strongly affecting the time period T and therefore has a more lasting effect on the inertial forces, mass scaling should be preferred.

Mass scaling means artificially increasing the mass of the model. Since the mass and density respectively has the important role of defining the time step for integration (see Equation 9 and 10 in Section 2.4.2), increasing the mass will enlarge the stable time increment Δt_{stable}. Hence the

analyses can be solved faster.

There are two possibilities of mass scaling in ABAQUS:

- To scale the mass by a certain factor.

- To scale the mass by defining a minimum stable time increment Δt.

As the FE model consists of elements of different sizes, a uniform scaling with a constant factor would increase the mass especially of the large elements too much. So we prefer the second possibility, where only the mass of these elements, whose stable increment Δt_{stable} is smaller than the defined one, is scaled. This is defined in ABAQUS with the type BELOW MIN for the option *FIXED MASS SCALING. Hence the mass of all those elements with a stable time increment $\Delta t_{stable} < \Delta t$ are automatically scaled by a corresponding factor so that their stable time increment is redefined as $\Delta t_{stable} = \Delta t$. As a result of this kind of mass scaling only portions of the model, where the smallest elements are located, are scaled. Nevertheless the user has to verify that the changes in mass and consequently the increase in inertial forces does not influence the results of the simulation significantly. This can simplest be done by comparing it to unscaled results.

Summarizing the goal of mass scaling is to determine which amount of scaling will provide reasonable results while saving as much computer calculation time as possible. However, mass scaling will always reduce the quality of simulation results.

3 Basic Geometry and Physics to be Modelled

3.1 Geometry

In this section we explain the defined geometrical data of the model. Due to using symmetric boundary conditions only one quarter of the defected pipe will have to be modelled (see Figure 4.1 in Section 4.1). Thus the following geometric data refers to the quarter plate or pipe respectively.

3.1.1 Geometry of the Pipe

To create a pipe model only two geometry parameters have to be defined, namely the outer diameter D and the ratio D/t of the diameter to the thickness of the wall. Specifically for oil pipelines the following dimensions depicted in Table 3.1 were chosen for modelling:

Diameter D	Ratio D/t
[mm]	[-]
400	20

Table 3.1: Pipe geometry data

Because the pipe is transferred from transferring a plate model, the plate's dimensions are also of interest. The plate's length L (which is equal to the pipe's length because only the cross section is transformed) is fixed by the modelling principle according to Zhang [2], that it should be at least three times the plate's width W:

$$L > 3\,W \tag{12}$$

Because finally we want to obtain the desired pipe dimensions, the plate's width W should be half the circumference $\frac{U}{2}$ of the pipe:

$$W = \frac{U}{2} = \frac{\pi\,D}{2} \tag{13}$$

So Equation 12 becomes:

$$L > 3\,\frac{\pi\,D}{2} \tag{14}$$

The pipe and the plate have the same thickness t and the other dimensions of the plate can be deduced by inserting the pipe values from Table 3.1 in Equations 13 and 14. Thus the plate was modelled with the numbers given below in Table 3.2. The value of the width W has to be specified exactly in order to gain a pipe with the desired diameter D, whereas the length L of the plate has only to fulfil Equation 14.

Length L	Width W	Thickness t
[mm]	[mm]	[mm]
1885.000	628.319	20.000

Table 3.2: Plate geometry data

3.1.2   Geometry of the Crack

Due to symmetry only half of the defect was modelled and a "canoe" shaped surface crack was conducted.. The crack was positioned on the upper edge in the y–z–plane in the local plate coordinate system. This is depicted in Figure 3.1:
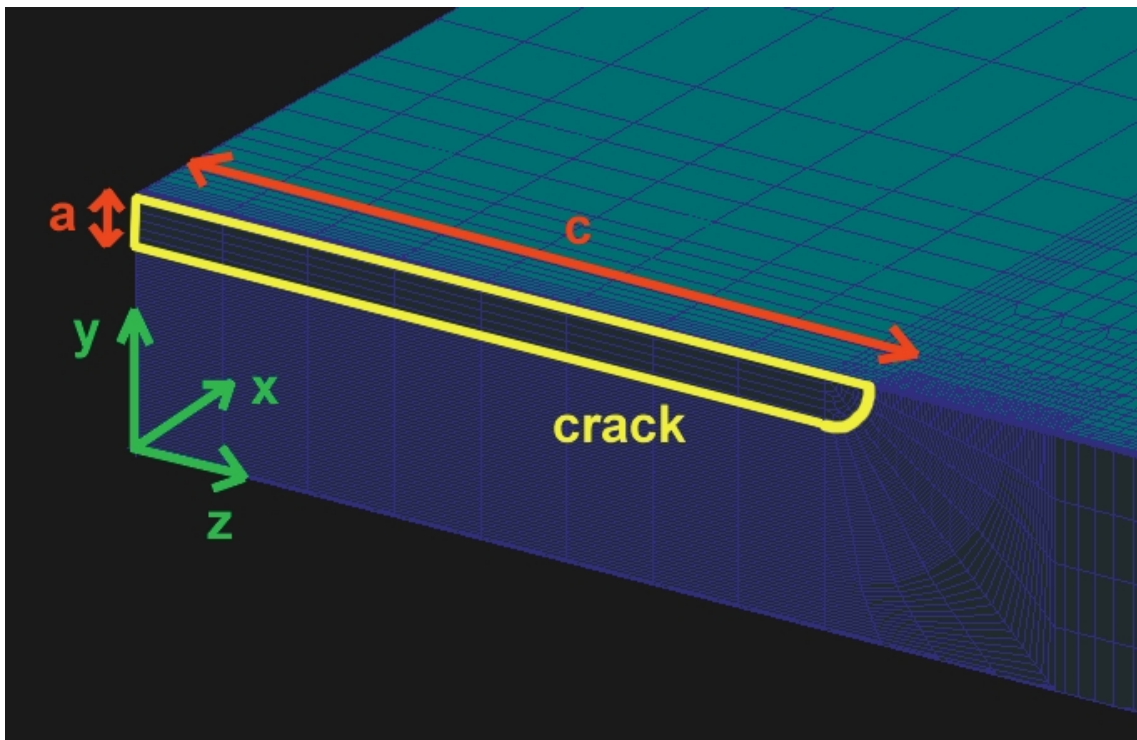
Figure 3.1: Overview of crack geometry

The crack was created by applying certain boundary conditions to the remaining material in the y–z–plane (see Section 3.4). The crack dimensions are those depicted in Table 3.3. These values result in a crack amounting to 10% of the pipe's circumference and 20% of the its wall thickness.

Crack length c	Crack depth a
[mm]	[mm]
64	4

Table 3.3: Crack geometry data

3.2   Material Properties

In all simulations an uniform material, namely X–65, was used. This material is a steel alloy often used in oil pipelines. Table 3.4 below gives an overview of the material properties. The implementing of the corresponding elastic-plastic material behavior in ABAQUS was explained in Section 2.3.1.

Young's modulus E [MPa]	Density ρ $\left[\frac{\text{t}}{\text{mm}^3}\right]$	Poisson's ratio ν [-]	Yield stress σ_y [MPa]	Hardening exponent n [-]
200000	7.8 E-09	0.3	460	0.07

Table 3.4: Material properties

3.3   Groups and Paths in the Model

For making it possible to apply boundary conditions to the model, several sets of nodes and elements have to be defined in PATRAN. Table 3.5 lists all used groups with their purpose and a description of which nodes or elements they contain. A visualization of the group's position is given in Figure A.1 to A.3 in Appendix A.

Group	Contains	Purpose
AONE	all nodes in the y–z–plane without the crack nodes	to apply symmetry boundary condition
ATWO	all nodes in the x–y–plane	to apply symmetry boundary condition
ATHREE	all nodes in the end plane opposite to AONE	to apply the load
AFOUR	all nodes in the end plane opposite to ATWO	to apply symmetry boundary condition for the pipe
NCTOD	first node above the crack front in the x–y–plane	to measure the CTOD value δ
NGLOB	node at the upper edge of the model where ATWO and ATHREE coincide	to measure the value of global displacement Δ
NFIX	node coincident with the origin of the local plate coordinate system	to fix the plate in the y–direction
BACK	element related to NGLOB	to measure the value of global strain ϵ

Table 3.5: Overview of groups

Due to having measurment of the global strain ϵ in only one element (BACK), a relative constant strain along the upper edge of the pipe was needed. In order to check, if the strain values in the elements along that edge are almost the same, a path was created there. That means that the strain can be printed out e.g. for all elements along path "M1", whereas the notation of the path gives the model number ($M1$ = path in Model 1, $M2$ = path in Model 2). Figure A.1-A.3 in appendix A show the location of this path in a pipe model.

3.4 Boundary Conditions

Due to using adequate symmetry conditions in the x–y– and y–z–plane, only one quarter of the full pipe has to be modelled. Thus the boundary conditions consist of symmetry conditions and of course the load.

3.4.1 Symmetry Boundary Conditions

In order to simulate a full pipe by only modelling a quarter of it, suitable symmetric boundary conditions have to be used. The pipe has two symmetry planes, namely the x–y– and the y–z–plane. Therefore, due to symmetry, the following boundary conditions are applied:

- x–symmetry for node set AONE ("X–SYMM" as boundary input).

- z–symmetry for node set ATWO and AFOUR ("Z–SYMM" as boundary input).

For simulating a plate in tensile loading the boundary must be changed to NFIX fixed in y–direction instead of z–symmetry for AFOUR due to set the model in space.

3.4.2 Load Boundary Condition

In the case of tensile load all nodes of node set AONE are fixed in x–direction while a certain displacement is applied to node set ATHREE on the other end of the pipe. This displacement should cause a global strain of $\epsilon = 0.05$, that is enough to obtain plastic deformation near the crack tip. Global displacement Δ and global strain ϵ are connected by the following equation, where L represents the model's Length (extension in x-direction):

$$\epsilon = \frac{(L + \Delta) - L}{L} = \frac{\Delta}{L} \tag{15}$$

From Equation 15 we can derive the value of the displacement: Out of Equation it arises that a displacement of

$$\Delta = L\,\epsilon = 1885 \text{ mm} \cdot 0.05 = 94.25 \text{ mm} \tag{16}$$

It has to be applied to node set ATHREE in positive x–direction.

4   Method

4.1   Problem Definition and Solving Method

Simulating ductile fracture of pipe sections with surface cracks consists of geometric modelling and implementing the material behaviour. For the geometric part it is only necessary to model a quarter of the defected plate and to apply appropriate symmetry boundary conditions (see Section 3.4.1). This process is schematically shown in Figure 4.1 and described in detail in Section 4.2.
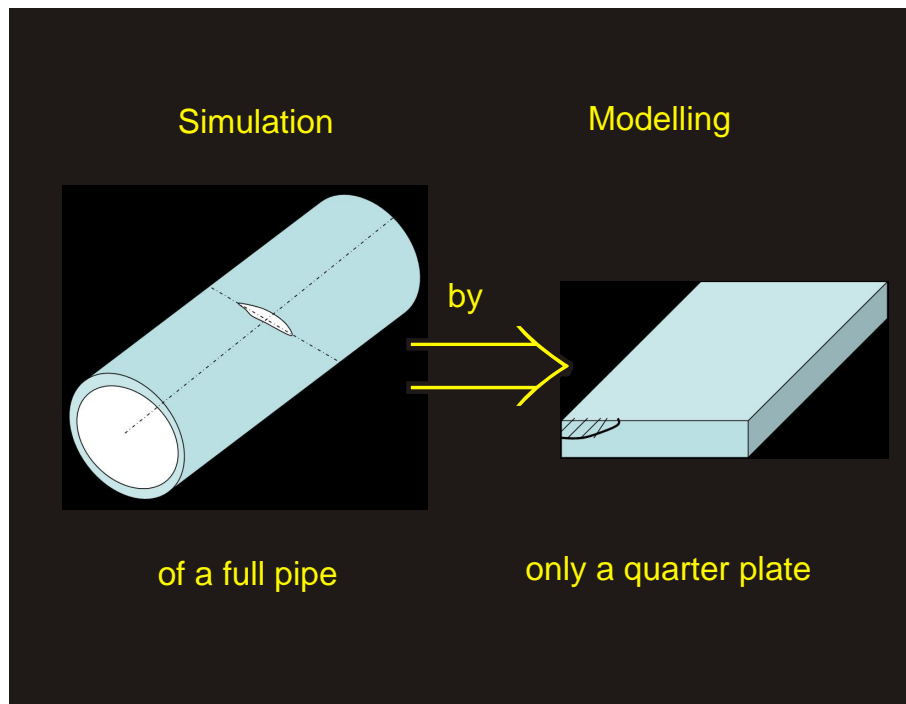
Figure 4.1: Simulation strategy (based on Zhang [2])

Besides the geometric modelling process, the second task is to simulate ductile fracture behaviour by implementing Gurson material. Since former tests at SINTEF to implement the Gurson routine for 3D models in ABAQUS Standard failed, we try a new approach: simulating in ABAQUS Explicit software. A first important step was to get to know the Explicit simulation procedure. As soon as the ductile fracture behaviour finally goes well for 3D models in Explicit simulations, we planned further trials in order to determine the influence of the gurson parameters and the force of varied geometrical crack data on ductile fracture behaviour.

The task was split into the following steps:

- At first we create a relative simple pipe model with a coarse mesh. On that model we study the Explicit simulation procedure. Finally we implement the Gurson material. Model 1 should be applied as a "simplified working model" and therefore we can not expect exact results.

- Based on the results of Model 1 we refine the mesh for Model 2. This new pipe model should now be able to provide reasonable results. Furthermore, we test the influence of the Gurson parameters on the ductile fracture behaviour with Model 2.

- With nearly the same model (now called Model 3) we vary the geometric crack data (crack length) in order to clarify the influence of that issue on ductile fracture.

4.2 Modelling Process

We created a pipe model for simulating ductile fracture behavior with several programs and assignment was split as follows:

1. Defining a system of units (see Section 4.2.1).

2. Creating the input files in PATRAN (see Section 4.2.2).

3. Transforming the plate model into a pipe in MS Excel (see Section 4.2.3).

4. Adding data to the input files in gVim (see Section 4.2.4).

5. Analysing the results in ABAQUS Viewer (see Section 4.2.5).

4.2.1 Defining a System of Units

Before starting any modelling step, we must define a system of units. Since PATRAN and ABAQUS have no built-in system of units, all input data has to be specified in a self consistent unit system. Due to easier manageability (especially for creating the model in PATRAN) the SI-system of mm was used throughout this project. Table 4.1 shows the relationship between the SI and the SI(mm) system.

Quantity	SI	SI(mm)
Length	m	mm
Mass	kg	t (10^3kg)
Time	s	s
Density	$\frac{kg}{m^3}$	$\frac{t}{mm^3}$
Force	N	N
Stress	Pa $\frac{N}{m^2}$	MPa $\frac{N}{mm^2}$
Energy	J	mJ

Table 4.1: Self consistent SI–systems

4.2.2   Creating the Input Files in PATRAN

For creating the input files we chose PATRAN because of its advantages in actuations with sets and in creating automatic mesh transitions. As mentioned before creating a FE mesh for a 3D pipe model was carried out by modelling only one quarter of a surface cracked 3D plate and afterwards transferring its coordinates into a pipe (see Section 4.2.3). For creating the plate mesh we realised the following dimensions according to Table 3.2 in Section 3.1.1. All over the model we used only 8–node brick elements (C3D8).

For an efficient modelling process we applied the following technique (see also Figure 4.2):

1. Creating a fine meshed core with revolved elements for the round part of the "canoe" shaped crack and surrounding prism elements.

2. Extruding with uniform elements against z–direction till the x–y–plane supplies the ligament.

3. Extruding of the present mesh till the final dimension at first in z– and finally in x–direction provides the remaining part.
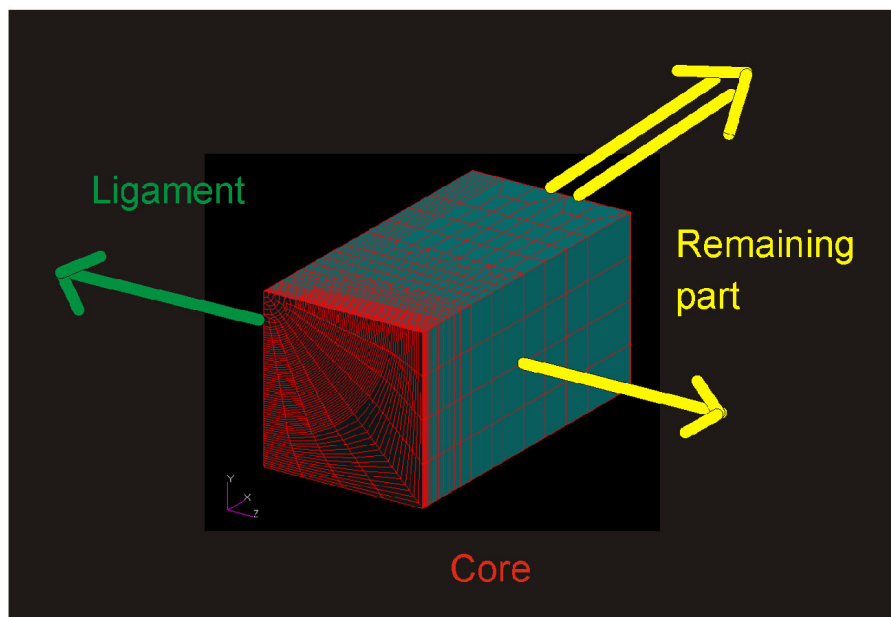

Figure 4.2: Extruding from the core

Special attention has to be focused on equivalencing elements in the remaining area next to the revolved ones in the core. Furthermore, prior consideration about the location of the transitions is essential, because they can be only used in one plane for a single element in 3D models.

The area where a fine mesh has to be used is of course in the ligament and in the core next to the crack plane where ductile tearing should occur. According to Chen/Lambert [4] the width h of the tearing zone (in x–direction) remains almost constant as the crack advances. So the fine meshed area has not to be extended all over the pipe. In this project a sufficient width of $h=6\,\text{mm}$ of the tearing zone was finally realised.

4.2.3   Transformation of the Plate into a Pipe

Because the dimensions of the plate model are calculated out of pipe dimensions (see Section 3.1.1) only a transformation of the y–z–cross section is necessary. This transformation can be conceived easily if the one end of the plate next to the crack is fixed and the other end is bended to a pipe. This simultaneously provides a convenient location of the local plate-coordinate system (I) in the global pipe-coordinate system (III). The following equations can be established after defining a local cylindrical coordinate system (II) in the x–y–plane with the same origin as the global pipe coordinate system (III). Figure 4.3 gives an overview of the coordinate systems and of the notation of the coordinates. Table 4.2 describes the positioning of the three coordinate systems. In Figure 4.3 the pipe and plate dimensions are also added, where D represents the outer diameter and t gives the thickness of the pipe while W is the plate's width.
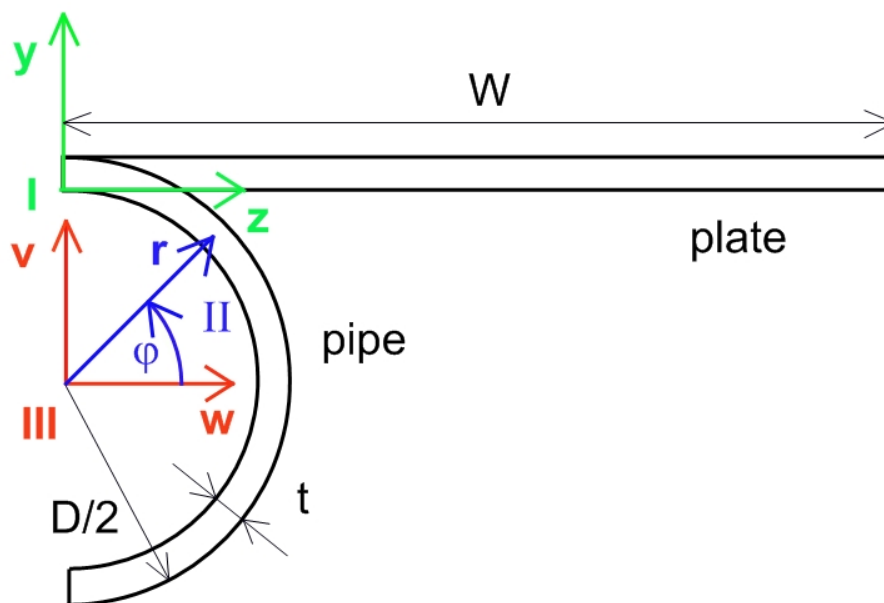

Figure 4.3: Overview of plate and pipe coordinate systems

We only used u, v and w here in this chapter to differentiate between plate and pipe coordinate system for simplicity. Against it in all other sections, x, y and z are also used for the pipe instead of u, v and w.

System	Related to	Type	Coordinates	Origin	Orientation
I	Plate	rectangular	x, y, z	in the ligament of the crack	all plate extensions are positive
II	Pipe	cylindric	r, ϕ	in the center of the pipe	middle of the canoe crack is located at $\phi = \pi/2$
III	Pipe	rectangular	u, v, w	in the center of the pipe	all pipe extensions are positive

Table 4.2: Overview of coordinate systems

The mathematical transformation passes through the following two steps:

1. The geometrical node data is converted from the plate coordinate system (I) to the cylindrical one (II). At first r can be expressed as a function of y by using the inner diameter d of the pipe:

$$r = \frac{d}{2} + y = \frac{D - 2\,t}{2} + y = \frac{D}{2} - t + y \tag{17}$$

Second, ϕ can be calculated from z, whereas W stands for the widthof the plate:

$$\phi = \frac{\pi}{2} - \left(\frac{z}{W}\right)\pi \tag{18}$$

2. The data must be transferred from the cylindrical coordinate system (II) to the global rectangular one (III). The rectangular coordinate v can be calculated from:

$$v = r\,\sin\phi = \left(\frac{D}{2} - t + y\right)\sin\left\{\frac{\pi}{2} - \left(\frac{z}{W}\right)\pi\right\} \tag{19}$$

while finally w is obtainable from:

$$w = r\,\cos\phi = \left(\frac{D}{2} - t + y\right)\cos\left\{\frac{\pi}{2} - \left(\frac{z}{W}\right)\pi\right\} \tag{20}$$

Equation 17 to 20 were implemented into MS Excel. The conversion from z to ϕ according to Equation 18 is once again displayed in Figure 4.4 for better understanding. We copied the geometrical data of the plate's nodes from the input files, transferred it into pipe coordinates by using MS Excel and re-embedded it in the input files. It was not necessary to apply any transformation to the third coordinate:
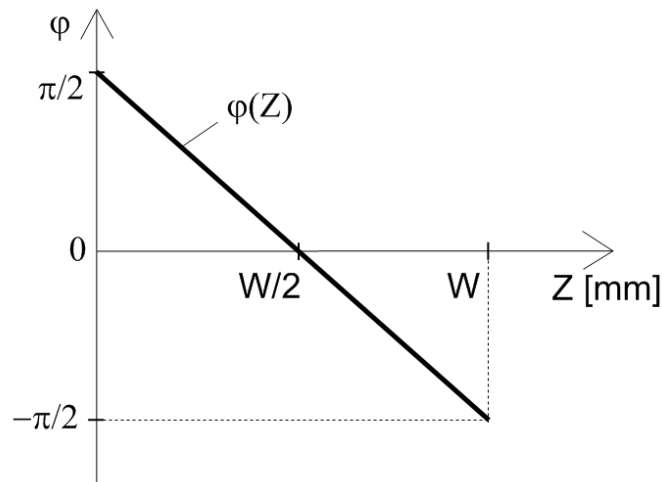
$$u = x \tag{21}$$

Figure 4.4: ϕ in addiction to z

It should finally be pointed out, that special attention must be paid to the final w–values of the nodes of group AFOUR. Due to rounding errors resulting from the multiplication by pi, these values are incorrect and therefore the transformation does not result in a proper pipe. But this can be easily prevented by e.g. adding an IF function in MS Excel.

4.2.4   Editing the Input Files

We produced the input files in PATRAN without any element properties or boundary conditions. Only geometric data from PATRAN for nodes, elements and groups of them was further used. Any other required input data was later added in gVim. We chose this text editor because of its advantageous syntax highlighting and its displaying input numbers in compendious blocks.

The following editing of the input files was done in gVim:

- Re-embedding the transferred geometric node data.

- Defining element type as C3D8 for Standard or C3D8R for Explicit calculations.

- Adding material properties (see Table 3.4 in Section 3.2).

- Adding boundary conditions (see Section 3.4).

- Adding Explicit simulation parameters (see Table 5.2 in Section 5.4.1).

- Defining the required output (stress, strain, displacement, reaction forces and void volume fraction).

4.2.5   Analysing the Results in ABAQUS Viewer

After having done all calculations in ABAQUS, we decided to process the results in ABAQUS Viewer. This tool has a better visualisation than PATRAN for producing graphs and especially figures and makes it easier to analyse the results.

We explain in the following how the values of crack growth Δa for determining crack resistance in chapter 7.2.3 were measured "manually":

Due to comparability to former results at SINTEF we defined crack growth by reaching critical void volume fraction f_c. So the limit of the "Contour" output for the void volume fraction f in ABAQUS viewer was put on that f_c-level. Then we counted the elements next to the x-y-symmetry plane which own a void volume fraction $f > f_c$ for each point in time. That means crack growth Δa was only measured in the middle of the whole crack. By multiplying the corresponding number of counted elements m with the element's length l_y in y-direction we could obtain the value of crack growth Δa:

$$\Delta a = m \, l_y \tag{22}$$

We implemented Equation 22 also in MS Excel and the graph crack growth versus time was re-imported in ABAQUS Viewer for further analysing.

5   Model 1 – Getting familiar with the Simulation Procedure

5.1   Purpose and Model Data of Model 1

For modelling the mesh of Model 1, we orientated on earlier pipe models at SINTEF[9]. It was produced according to Section 4.2.2 and consists of 10880 elements. The smallest element of the crack tip region was chosen to have a length of $l_y = 0.25$ mm and the boundary conditions for the plate and the transferred pipe in tensile load case were applied (see Section 3.4).

5.2   Model 1 in ABAQUS Standard

As first step in this project we run the surfaced cracked plate in ABAQUS Standard. Afterwards we transferred it into a pipe (see Section 4.2.3) and calculated this model also by ABAQUS Standard. These results should give an impression, how the global behaviour of Model 1 corresponds with earlier results from stationary calculations without crack growth at SINTEF [9] (throughout this report denoted as "Given results"). Foremost as a basic principle, we had to check the simulation results of the plate and the pipe with respect to the following aspects:

- Receiving an uniform strain of around $\epsilon = 5\,\%$ nearly all over the model.

- Obtaining a strain concentration only near the crack tip.

- Getting a stretched pipe with a diminuated cross section.

We achieved the above listed points well. The obtained strain dispersal of Plate 1 is illustrated in Figure A.4 in Appendix A and we controlled visually the deformation of the Pipe 1 by superimposing deformed and undeformed shape (see Figure A.5 also in Appendix A).

Now we could compare the results for CTOD versus global strain (see Figure 5.1). They show that there is no difference between plate and pipe run in ABAQUS Standard for crack opening behaviour. It is also possible to see that Model 1 follows the expected "Given results" values in the first part of the analysis well. But with increasing strain, the CTOD values rise linearly instead of tending more upwards. But for now these results were satisfying enough.

5.3   Determining the Explicit Parameters

5.3.1   Determining the Time Period of the Analysis

In order to get familiar with the simulation procedure in ABAQUS Explicit, we first ran a simulation of Pipe 1 with simple elastic–plastic material in that software.

Based on observations in Section 2.4.3 a almost constant global strain dispersion like in ABAQUS Standard should be reached. So extensive testing with the total time period T was done. Starting
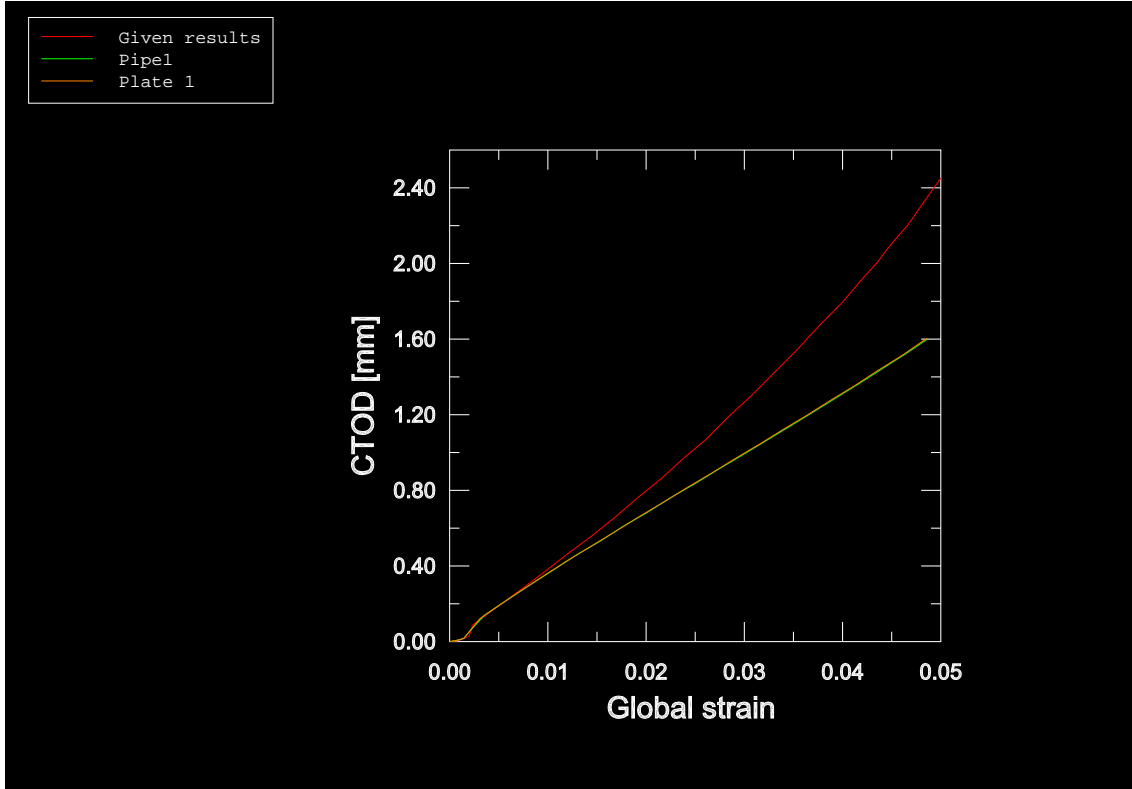
Figure 5.1: CTOD versus global strain for Plate 1 and Pipe 1

at the theoretical minimum of $T = 4$ ms according to equation 11 and finally increasing up to $T = 100$ ms should provide clarification of that issue.

Figure 5.2 shows the influence of the total time period T on the global strain dispersion. On the x-axis the x-coordinate values for the elements along the path "M1" (see Section 3.3) are given and the last index at the name indicates the duration of the applied total time period T in ms. It is obvious that a longer total time period of the simulations improves the dispersal of strain towards being constant and that the originally in Section 2.4.2 calculated length of $T = 4$ ms is totally insufficient. For now a time period of $T = 40$ ms seems to deliver an adequate constant strain dispersal but later influences of mass scaling and the implemented Gurson material led to a final simulation time period of $T = 100$ ms. So we added the results for Pipe 1–100 for comparing purposes in Figure 5.2.

5.3.2   Influence of Mass Scaling

To get an imagination of the value of the stable time increment Δt of the elements in Model 1, an unscaled simulation with putting out Δt (identifier "EDT" in the element output) of each element was realised at first. The time period T for this analysis can be set very short, since only the results of the stable time increment Δt (which are independent of the time period T) are of interest, and therefore a lot of calculation time can be saved. For obtaining this information, an unscaled run of Pipe 1–010 with a time period of $T = 10$ ms was realised.
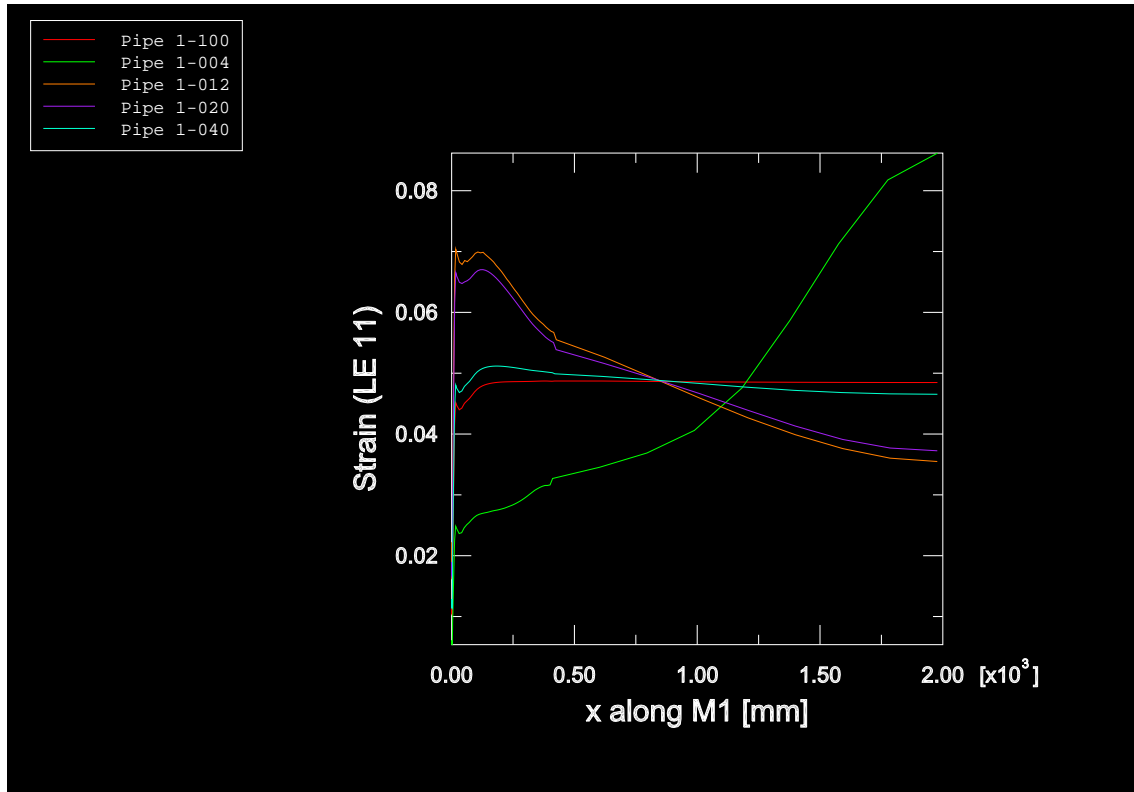
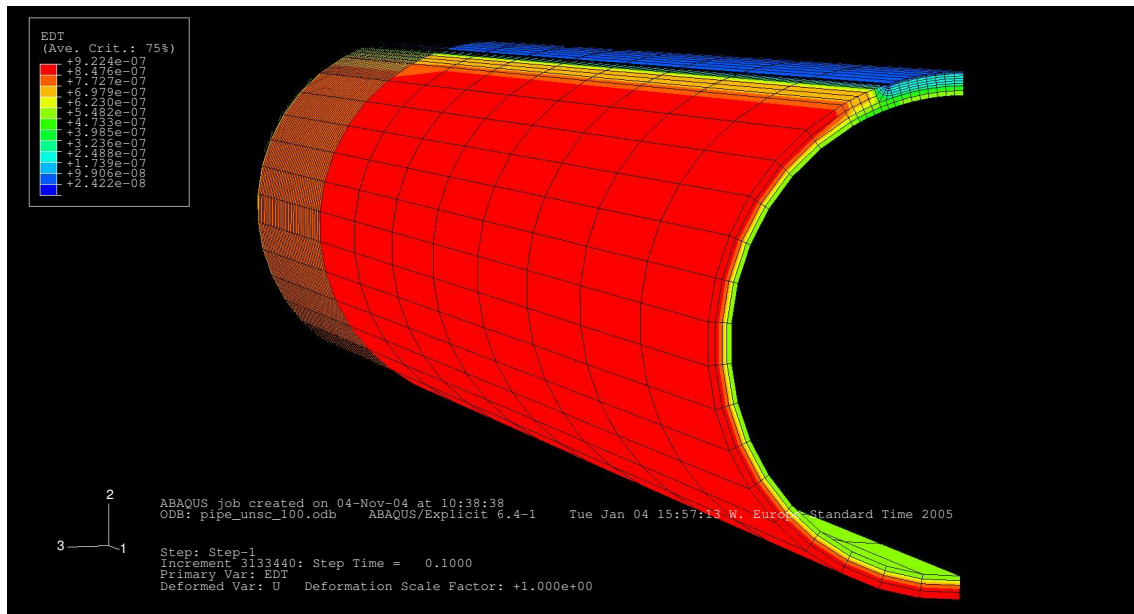Figure 5.2: Strain dispersion along Path M1 for Pipe 1

Figure 5.3: Stable time increments for all elements in Model 1

It can be seen in Figure 5.3 that large regions of Pipe 1–010 have an unscaled stable time increment of $\Delta t = 9$ E-06 s. So fixed mass scaling (see Section 2.4.4) with a minimum stable time increment $\Delta t = 1$ E-06 s will still surely provide reasonable results.

In order to proof that and to receive greater knowledge of the influence of mass scaling we realised large testing by varying the smallest stable time increment Δt. For the time period of the analysis we chose a value of $T = 40$ ms and the minimum stable time increment ranged between 5 E-07 s $< \Delta t < 5$ E-06 s. At first we checked the kinetic energies of the simulations, whether exceeding the limit of $5\,\%$ of the internal energy (see Section 2.4.3 for explaination).
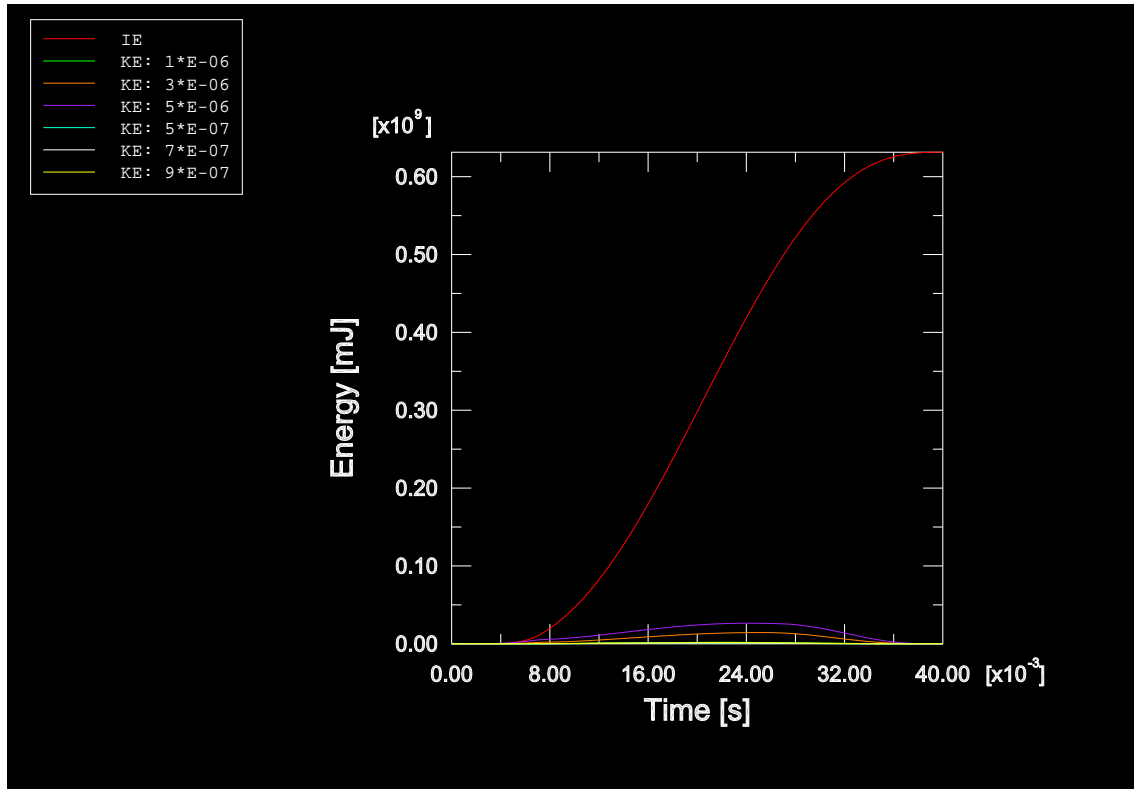

Figure 5.4: Comparing internal and kinetic energy of Model 1 for several mass scaling

In Figure 5.4 "IE" represents the internal energy and "KE" the kinetic energy of the whole models, while the minimum stable time increment is also given by the notation. There is only one of the internal energies displayed, because they are equal for all tested versions. It is obvious that at all mass scaling with a minimum stable time increment of $\Delta t > 1$ E-06 s there is a negligible amount of kinetic energy in the model ("KE" $< 0.05 \cdot$"IE"). For the other cases, where an marked amount of kinetic energy is there. Even though it is smaller than $5\,\%$, for this cases advanced consideration is necessary.

Therefore we summed up the reaction forces (load) in axial direction at the end of the pipe (element set ATHREE) and compared them. But we realised these simulations with a time period of $T = 100$ ms. This testing with a longer time period T was due to proving the rationality of later

analyses with implemented Gurson material, where such a time period of $T = 100$ ms was required.
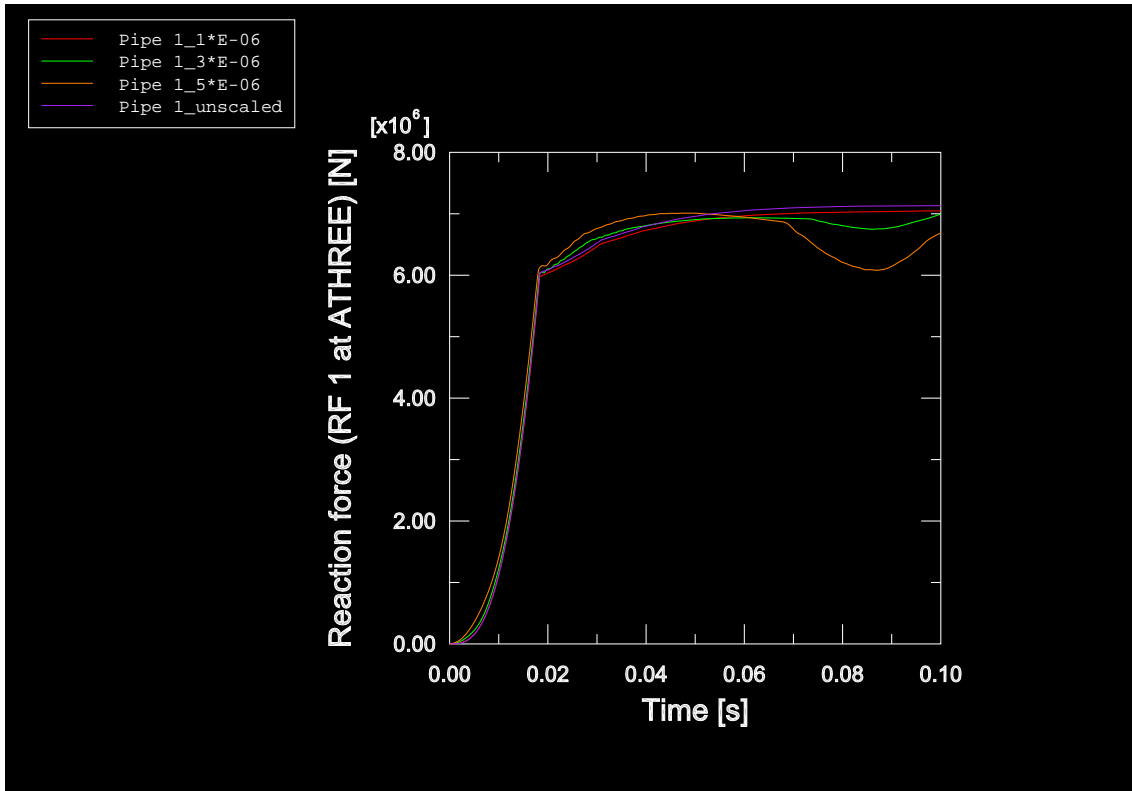

Figure 5.5: Comparing reaction forces of Model 1 for several mass scaling

Figure 5.5 shows the results of the reaction forces at the end of the pipe. They indicate that only the curve for a simulation with a minimum stable time increment of $\Delta t = 1$ E-06 s sensibly follows the unscaled results even though the values are a bit less. For mass scaling with a minimum stable time increment $\Delta t > 1$ E-06 s the ascertained results show, that this mass scaling is too high.

An unscaled simulation can probably not be run for any sophisticated model, because computer time will increase infinitely; e.g. nearly 3 days were required to solve a simulation of Model 1 without any mass scaling. Table 5.1 gives an overview of the computer time which is needed to run several simulations of Model 1 with the same time period of $T = 100$ ms and different reasonable mass scaling.

Δt [s]	5 E-07	7 E-07	9 E-07	1 E-06
Computer time [h:min]	2:45	1:59	1:33	1:19

Table 5.1: Computer time for different mass scaling

Because computer time increases once more by implementing Gurson material a minimum stable time increment of $\Delta t = 1$ E-06 s was chosen for further analyses with Model 1.

As the last point in the investigation in Explicit simulation parameters we clarified the influence of mass scaling on the strain dispersal. This was done during the analyses with a time period of

$T = 40$ ms, because an insufficient strain dispersal would have caused further increasing of the time period T. This happened indeed, but was also affected among others by later implementing of the Gurson material.
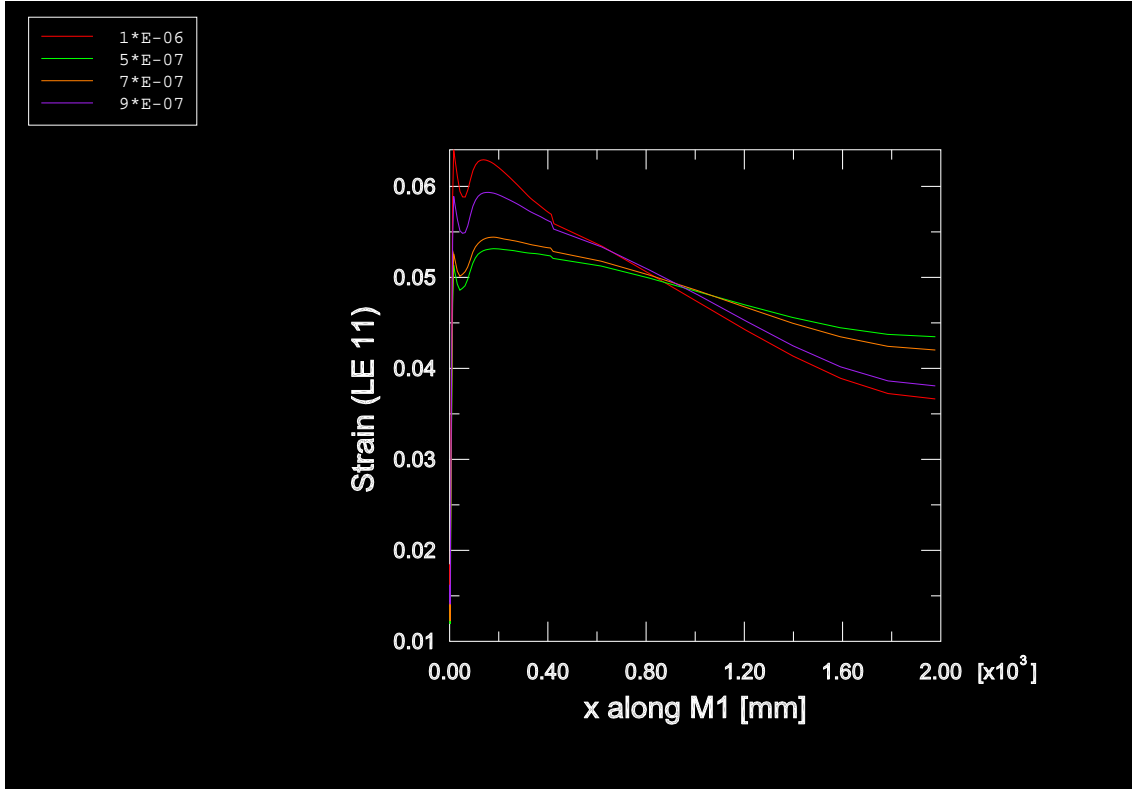

Figure 5.6: Comparing strain dispersal of Model 1 for several mass scaling

In Figure 5.6 the elements' strain in x-direction (LE 11 = ϵ_{11}) is given along the path $M1$, which is located along the upper edge of the half pipe. The graph outlines, that higher mass scaling, which equals defining a smaller minimum stable time increment Δt, impairs the strain dispersal.

In summary it can be said, that working without mass scaling is not possible due to time inefficiency. So for defining a reasonable minimum stable time increment the following procedure should be executed:

1. Running an unscaled simulation with a short time period T to get an impression of the value of the stable time increment Δt of the elements all over the model.

2. Choosing a value for the minimum stable time increment Δt for mass scaling which is not much larger than it is in large parts of the model.

3. Checking the scaled results, whether the amount of kinetic energy is negligible in comparison to the internal energy of the model.

4. Comparing the load results of the scaled simulations with unscaled onces for the same time period T for verifying the results, if this is possible.

5.4   Implementing the Gurson Material

5.4.1   Simulation Parameters

By implementing Gurson material the crack should now be able to grow at first in direction to the center of the pipe and then in circumferential direction. Based on observations in Section 2.3.2 we used the following Gurson parameters for simulating ductile crack growth with Model 1:

f_0	f_c	f_F	T	Δt
[-]	[-]	[-]	[s]	[s]
0.005	0.030	0.160	0.1	1 E-06 s

Table 5.2: Simulation parameters for Model 1

Table 5.2 gives an overview of the values for the time period T and the smallest stable time increment Δt, which were realised in these simulations.

5.4.2   Crack Growth

Crack growth can be easily visualized with the STATUS output in ABAQUS. All elements, which have failed by reaching void volume fraction of final failure f_F and consequently lost any stress carrying capacity, are plotted in another colour in that output type. It should be pointed out here that, if the elements have failed once, they can be distorted very easily. So scanning the results in an undeformed plot modus is advantageous.

Achieved from Picture Sequence 1 in Appendix B, where the failed elements are plotted in blue colour, three significant crack growth events for Model 1 are listed below in Table 5.3. The appropriate values for global strain ϵ for T_1,T_2 and T_3 were taken out from Figure A.7 in Appendix A and these for global displacement Δ, which were obtained from Figure A.8 also in Appendix A (which is nothing else than the applied smooth amplitude in ABAQUS Explicit), were also added.

Event	Point in time τ	Global strain ϵ	Global displacement Δ
	[s]	[-]	[mm]
Crack growth initiation T_1	0.053	0.027	51
Through crack T_2	0.070	0.039	78
Final pipe failure T_3	0.081	(0.037)	89

Table 5.3: Overview of crack growth events

Initiation of crack growth T_1 happens, when the first element next to the x–y–plane fails. Then the crack is at first growing in circumferential direction till the core, whereas only the crack front ligament elements next to the y–z–plane are failing. After that the crack extends among

maintaining a "canoe" shape in direction to the center of the pipe. So through crack T_2 is defined when the crack reaches the inner diameter d of the pipe. In the end final fracture of the pipe T_3 transpires, when all pipe elements next to the crack plane (y–z–plane) have failed. Since global strain ϵ does not increase further after through crack T_2, the strain value ϵ_3 for final failure of the pipe should be neglected.

5.4.3   CTOD Results

After ascertaining crack growth data we eyed the results for CTOD versus global strain. Figure 5.7 shows these values and elaborates once again on the influence of mass scaling.
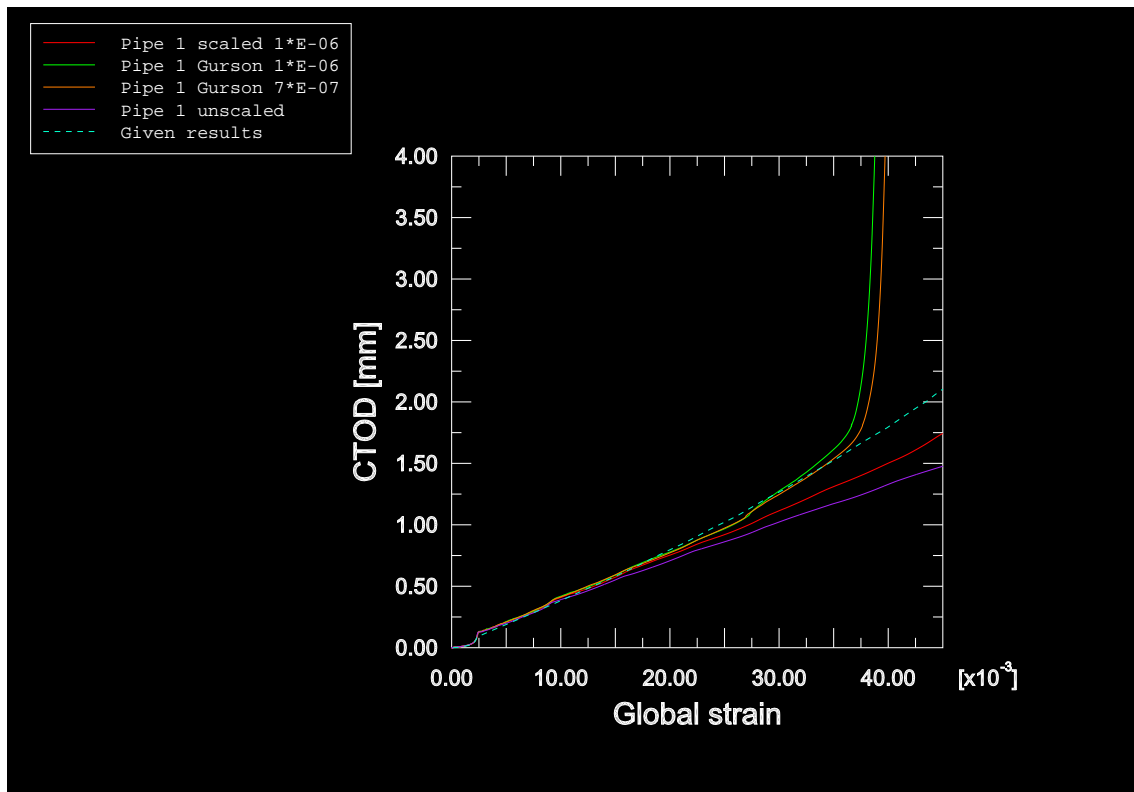
Figure 5.7: CTOD versus global strain for implemented Gurson material

In Figure 5.7 it is possible to see that Pipe 1 with implemented Gurson material provides good results compared with former stationary simulations without crack growth. Exactly when the first elements fails at $\tau_1 = 0.053$ s and correspondent global strain of $\epsilon_1 = 0.027$ is reached, the rise of the curve of "Pipe 1 Gurson" increases and it tends abruptly to infinity short before through crack (T_2 at $\epsilon_2 = 0.039$) is reached.

Ductile tearing, that is when the value of CTOD starts to rise, starts of course too late at $\epsilon_1 = 0.027$. This is however caused by a too rough mesh in the ligament, where the strain spreading is not well simulated.

By comparing the CTOD values for the two pipes with and without Gurson material and a minimum stable time increment of $\Delta t = 1$ E-06 s it is obvious that the added Gurson material has a comparable influence to mass scaling on the strain dispersal. It impairs the strain dispersal, thus leads to less strain in the element where it is measured (ELBACK) and therefore lifts the CTOD curve in the graph upwards.

We also determined the influence of using different mass scaling at the same Gurson parameters. This is likewise displayed in Figure 5.7. Due to unequal strain after crack growth initiation T_1 the results of the pipe with less mass scaling ("Pipe 1 Gurson 7*E-07") are a bit shifted to the right beginning from there.

5.4.4 Load Results

In order to get knowledge about the load carrying behaviour of the cracked pipe, we measured the reaction forces on both end planes of the pipe (AONE and ATHREE) and summed them up for comparison. While Figure A.6 in Appendix A shows the load versus global displacement behaviour over all the time period T of the simulation, Figure 5.8 below focuses against it on the interesting part beginning from $\tau = 0.7$ s, where the values are unequal. In Figure A.6 it is also possible to see that the implemented Gurson material slightly decreases the values of the load in comparison to a pipe with normal elastic-plastic material ("Pipe scaled 1*E-06").
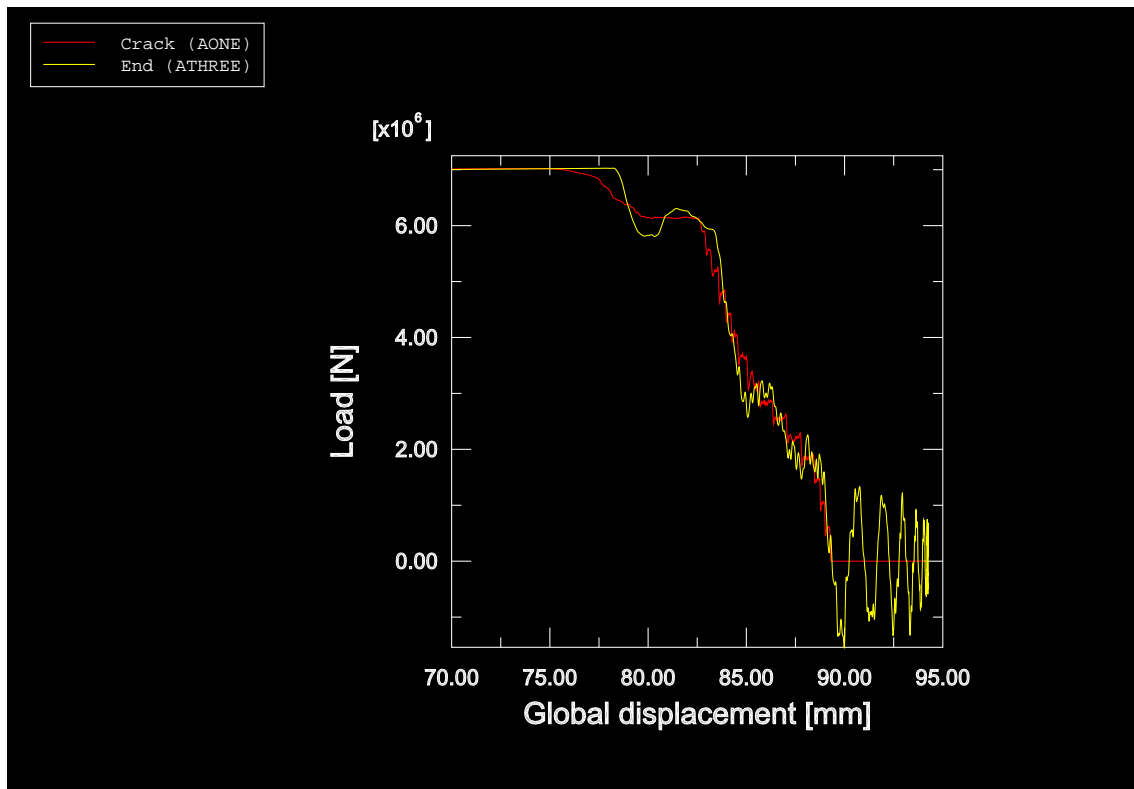
Figure 5.8: Load versus global displacement for implemented Gurson material

At first it should be summarised that the results of the load at the two ends are equal during the first 70 % of the analysis. Then the curves start to differ, which is shown in Figure 5.8. In oder to understand what is following now, the connection between crack growth events and load behaviour, which is given in Table 5.3 in Section 5.4.2, must be considered. The load at the crack plane (AONE) starts to decrease while the load on the other end remains still stable. Than a sudden load drop happens at the end plane (ATHREE) simultaneously to reaching through crack (T_2). After staying stable for a short period (at least the load on the crack plane) both loads fall off to zero until final pipe failure (T_3) takes place. The load on the end plane covers large oscillations whereas the load on the crack plane stays reasonably constant at zero.

The small decrease of the load on the crack plane before through crack T_2 happens can be explained by less remaining cross section area owing to failed elements. But for illuminating the oscillations on the end plane after through crack, we had to combine the knowledge about crack growth with the results of kinetic energy in the model. In the same gasp we want to clarify the influence of mass scaling on that issue.
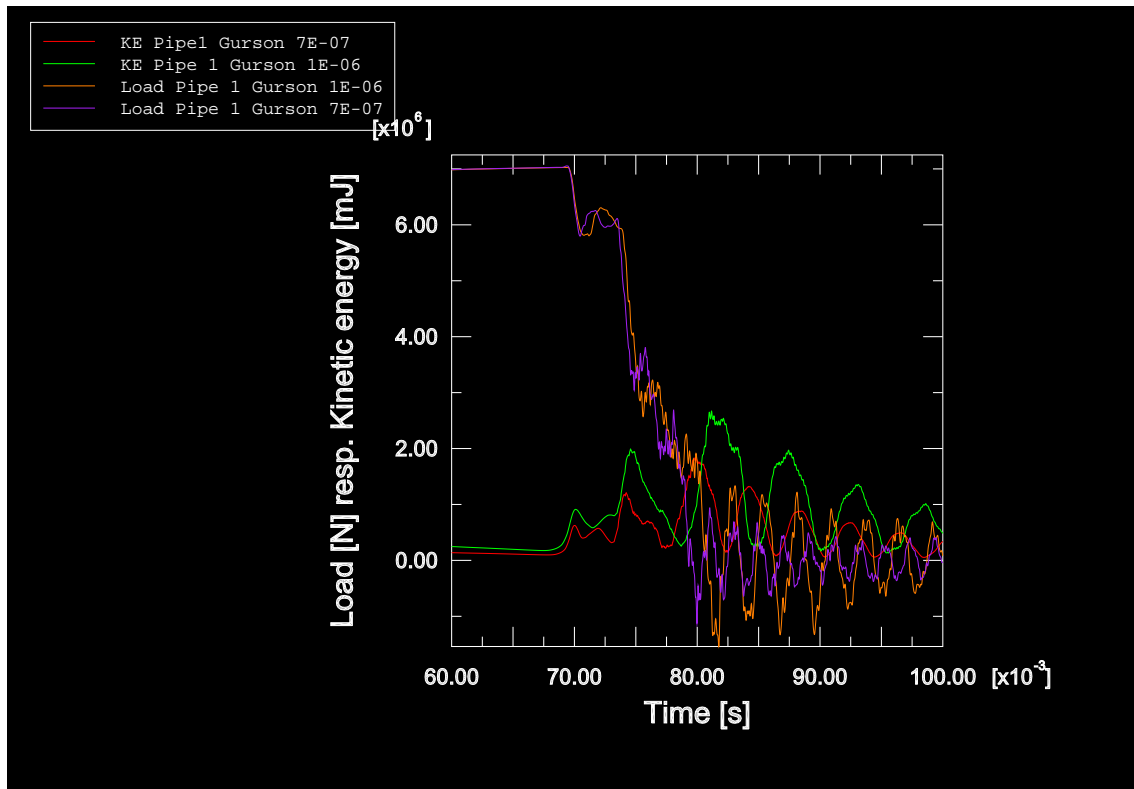
Figure 5.9: Load and kinetic energy versus time for different mass scaling

Consequently we run two models of Pipe 1 with the same implemented Gurson material but with different applied mass scaling (Δt is given by the marking). The data of the load on the end plane of the pipe (ATHREE) and of the kinetic energy of the model (marked "KE") were collected and are displayed against time in Figure 5.9. It becomes obvious that the kinetic energy of the whole

model suddenly rises when through crack is reached. This indicates that starting from that point in time dynamic effects are involved in the simulation. They are caused by the sudden deletion of the just failed elements on the crack plane and are amplified by mass scaling, where higher mass scaling is more increasing the oscillations in kinetic energy as well as on the load. The influence by mass scaling on the dynamic effects is carried through the whole pipe and is boosted measurable at the end plane (ATHREE). Since the simulations are quasi–static, we expected dynamic effects like the occurred oscillations.

5.5 Compendium of Results of Model 1

At first we determined the parameters for a quasi-static simulation with Model 1. Furthermore simulating ductile fracture behaviour by implementing Gurson material in ABAQUS Explicit worked well. But due to the simplicity of Model 1 the results are not exact.

So for improving the results, especially obtaining ductile tearing much earlier, we need to consider about the strain behaviour near the crack tip:

Figure A.9 in Appendix A shows the strain extension near the crack tip for Plate 1. It shows that the strain spreads non–uniformly downwards from the crack tip with an angle of about 45 degree. All over that region the strain dispersal in the new model should not be hampered any more by a refined mesh. So we decided the following improvements for creating the new mesh of Model 2:

- A finer mesh in the ligament until $x = 20$ mm should be realised.

- The crack ligament elements' length in x-direction l_x should get smaller (in order to obtain a quadratic element shape we changed from $l_{x1} = 0.5$ mm to $l_{x2} = 0.25$ mm).

6   Model 2 – Determining the Influence of the Gurson Parameters

6.1   Purpose and Model Data of Model 2

Based on experience with Model 1 we implemented the decided mesh improvements in Model 2. With that model it should be possible to produce reasonable results including an earlier start of ductile tearing. If that works well, the influence of the Gurson parameters should be detected.

We produced Model 2 comparable to Model 1 (same shape and extension). Model 2 consists of 20893 elements and in the crack ligament we realized a quadratic element size of $l_x = l_y = 0.25$ mm. The fine mesh was extended to $x = 20$ mm and the elements out of that area were now differently produced from Model 1. There we defined a constant element length, whereas now the ONE–WAY–BIAS function in PATRAN was utilised in order to obtain a gradually growing mesh starting from the tearing zone.

6.2   Preliminary Work with Model 2

The first point to check was, whether the refined mesh yields to a better strain carrying capacity in the crack ligament. This we checked already for Plate 2 run in ABAQUS Standard in order to prevent further work of no avail. Figure A.10 in Appendix A shows a much smoother strain spreading in the ligament as for Model 1 (see Figure A.9 in Appendix A). These two figures also conspicuously display the redefined mesh in the ligament. Because these results of Model 2 were satisfying, we tackled further work, that is to say defining the Explicit parameters.

Since Model 2 has the same dimensions as Model 1, the same time period of $T = 100$ ms was chosen. We passed through the procedure to define mass scaling as mentioned in Section 5.3.2 with the following results:

1. The short unscaled simulation of Model 2 outlines, that there is a stable time increment $\Delta t = 7$ E-07 s in large regions of the model (see Figure A.11 in Appendix A).

2. Checking the scaled results in relation to the amount of kinetic energy in comparison to the internal energy of the model displays that there is only an influence for $\Delta t = 3$ E-06 s and $\Delta t = 5$ E-06 s (see Figure A.12 in Appendix A).

3. Comparing of the load results was only done for the scaled simulations among each other, because we could not run an unscaled model due to infinite large required computer time. But the results (see Figure A.13 in Appendix A) verify that the largest possible value for the minimum stable time increment is $\Delta t = 1$ E-06 s.

So we realised a convenient value of $\Delta t = 1$E-06s for the minimum stable time increment for mass scaling of Model 2. This decision enabled to compare the results of Model 2 with Model 1 without

being so much influenced by mass scaling. Furthermore we used the same Gurson parameters as for Model 1 initially for Model 2 (see Table 5.2 in Section 5.4.1).

6.3 Comparison Model 1 – Model 2 for implemented Gurson Material

In this step we compared the results of CTOD versus global strain and load versus global displacement for Model 1 and 2. This should clarify the influence of the finer mesh on ductile fracture behaviour by using the same Gurson parameters.

6.3.1 Comparison of CTOD Results of Model 1 and Model 2

At first we compared the results for CTOD versus global strain. Figure 6.1 shows that Model 2 follows exactly the results of Model 1 until reaching global strain of $\epsilon = 0.008$. Then the results of Model 2 follow the "Given results" more closely than Model 1 until global strain of $\epsilon_1 = 0.018$ is reached, where crack growth initiation happens for Model 2. Now the CTOD values start to indicate the same shape of increasing for the crack growth period as for Model 1. This earlier start of crack growth at a global strain of $\epsilon_1 = 0.018$ in Model 2 is much more reasonable than the value of $\epsilon_1 = 0.027$ at Model 1. So in summary it can be said, that the point in time when crack growth starts is influenced by a finer mesh but the crack growth itself is not.
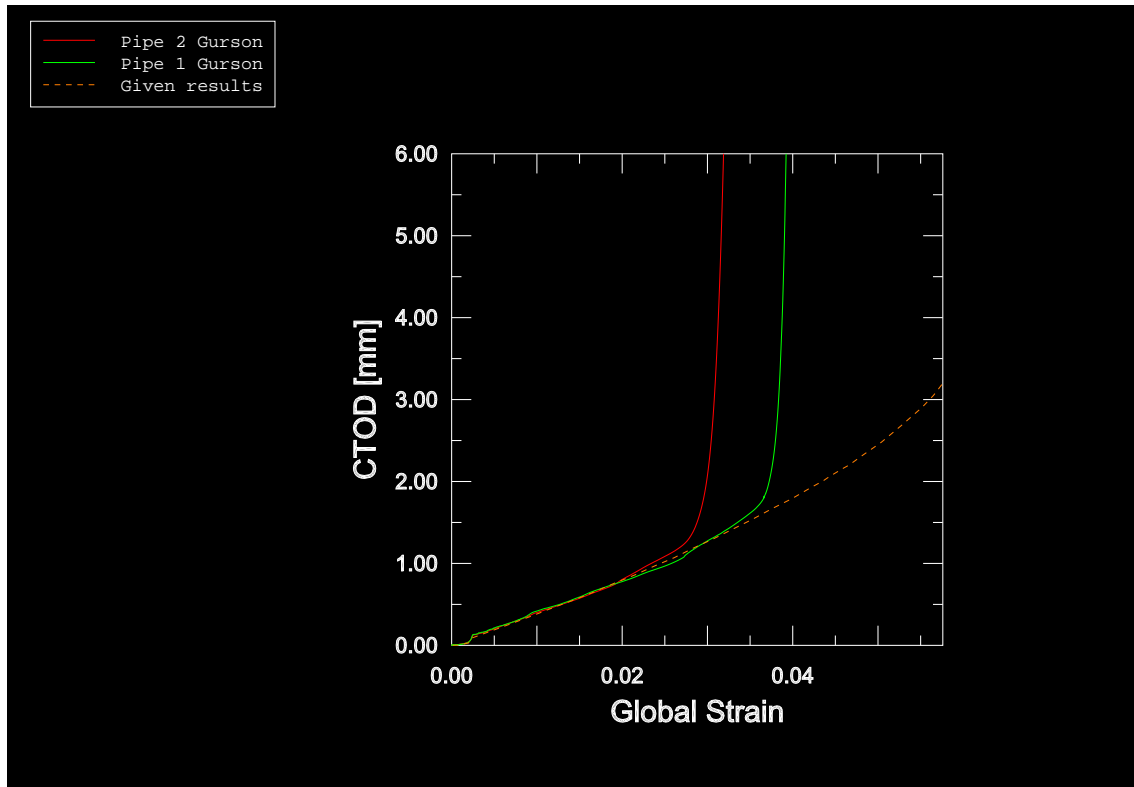
Figure 6.1: Comparing CTOD versus global strain for Model 1 and Model 2

6.3.2   Comparison of Load Results of Model 1 and Model 2

As a second point the load versus global displacement graphs are likened. Figure 6.2 shows that the load for Model 2 does not reach the same value as for Model 1. This differing in quantity of the results occurs due to mass scaling. Although the same minimum stable time increment of $\Delta t = 1\,\text{E-}06\,\text{s}$ was utilized the influence of mass scaling is much higher in Model 2, because there are much more small elements, which are scaled indeed.
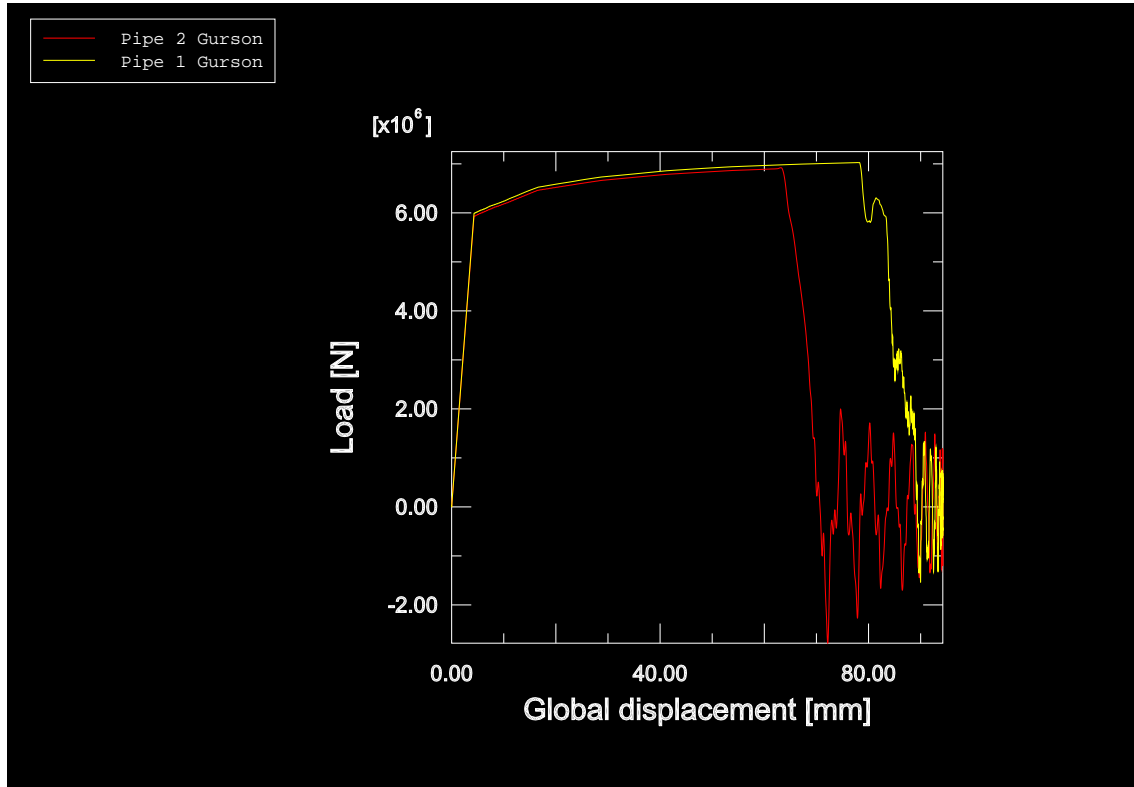
Figure 6.2: Comparing load versus global displacement for Model 1 and Model 2

The basic shape for the two curves is the same. Only initiation of crack growth and consequently the sudden load drop occurs earlier for Model 1. Also the small "constant" part (at a global strain of about $\epsilon = 0.80$, where the large oscillation is visible) of the curve of Model 1 after reaching through crack is not any more ascertainable for Model 2. And the load values of Model 2 are more straightly going downwards to zero without covering any large oscillations. They start foremost after reaching final pipe failure. So it can be summarised, that these differences in the graphs are most likely caused by rough mesh transitions in Model 1.

6.4   Influence of the Gurson Parameters on the Crack Growth Behaviour

In this step of the project we scrutinised, whether the crack growth behaviour can be influenced by changing the Gurson parameters. It makes only sense to verify the initial void volume fraction f_0 and the critical void volume fraction f_c, cince the void volume fraction of final failure f_F is

dependent on f_0 (see Section 2.3.2) .

6.4.1   Influence of the Initial Void Volume Fraction

At first we examined the influence of a varied initial void volume fraction f_0. To change that parameter implies to add more or less voids to the initial material. So initiation of crack growth T_1 should of course happen earlier or later. But s the special point of interest is, whether the crack growth behaviour after that event will be still the same.
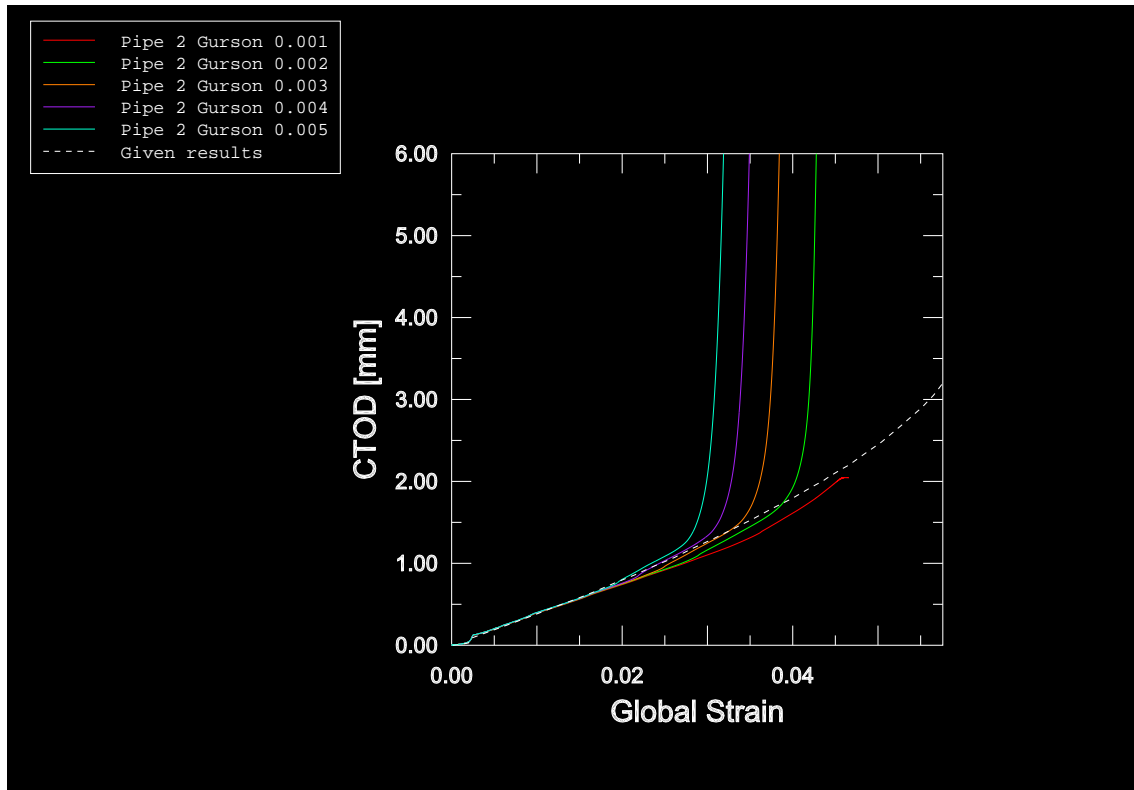
Figure 6.3: CTOD versus global strain for several initial void volume fraction

Figure 6.3 shows obviously that varying the initial void volume fraction f_0 has no influence on the fundamental shape of the CTOD versus global strain curves. All curves trend together until reaching the different crack initiation points T_1. This happens as predicted earlier or later in time or at smaller or larger strain respectively for the particular cases. But there is no influence on the crack opening behaviour after that event, because all curves own the same regime by tending to infinity.

Also the graphs of load versus global displacement in Figure 6.4 do not show any important difference for crack opening behaviour besides the different points in time of initiation.

It should be mentioned, that the highest load values occur of course at the model with the least initial void volume fraction f_0, where the material is fewest damaged at the beginning of the simulation. But apart from that the results lie together until reaching through crack and then
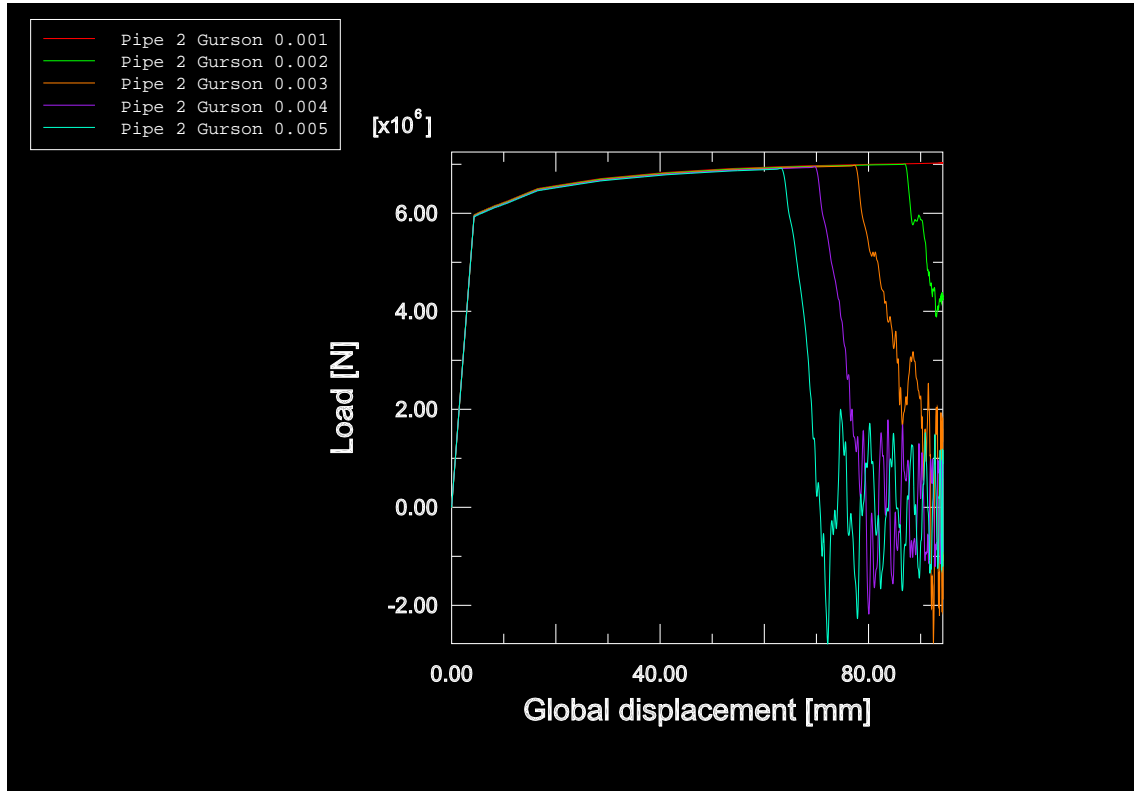
Figure 6.4: Load versus global displacement for several initial void volume fraction

tending downwards. At an initial void volume fraction of $f_0 = 0.001$ and $f_0 = 0.002$ the pipes do not reach final failure. This is caused by the applied smooth amplitude, where loading is not increasing enough in the end of the analysis.

So we can sum up that varying the initial void fraction f_0 only leads to an earlier or later crack growth initiation in time. This is expressing as a parallel shunting along the x-axis of the intense rising parts of the curves. But changing f_0 has also no influence (like varying f_0) on the crack opening behaviour after crack growth initiation.

6.4.2   Influence of the Critical Void Volume Fraction

After transpiring that the initial void volume fraction f_0 has no influence on the shape of the rise of the CTOD versus global strain results after crack growth initiation, we were interested, whether a changed critical void volume fraction biases that part of the graphs anyway. Consequently we varied the critical void volume fraction was variegated between $0.02 < f_c < 0.04$ at an constant initial void volume fraction of $f_0 = 0.002$.

Figure 6.5 shows that the shape of the strongly increasing CTOD curve after crack growth initiation is again the same for models with varied critical void volume fraction f_c. We can also see the same shunting along the x–axis as for a varied initial void volume fraction f_0. So we must sum up that a varied critical void volume fraction f_c only influences the point in time when crack growth is starting but not the crack growth behaviour after it.
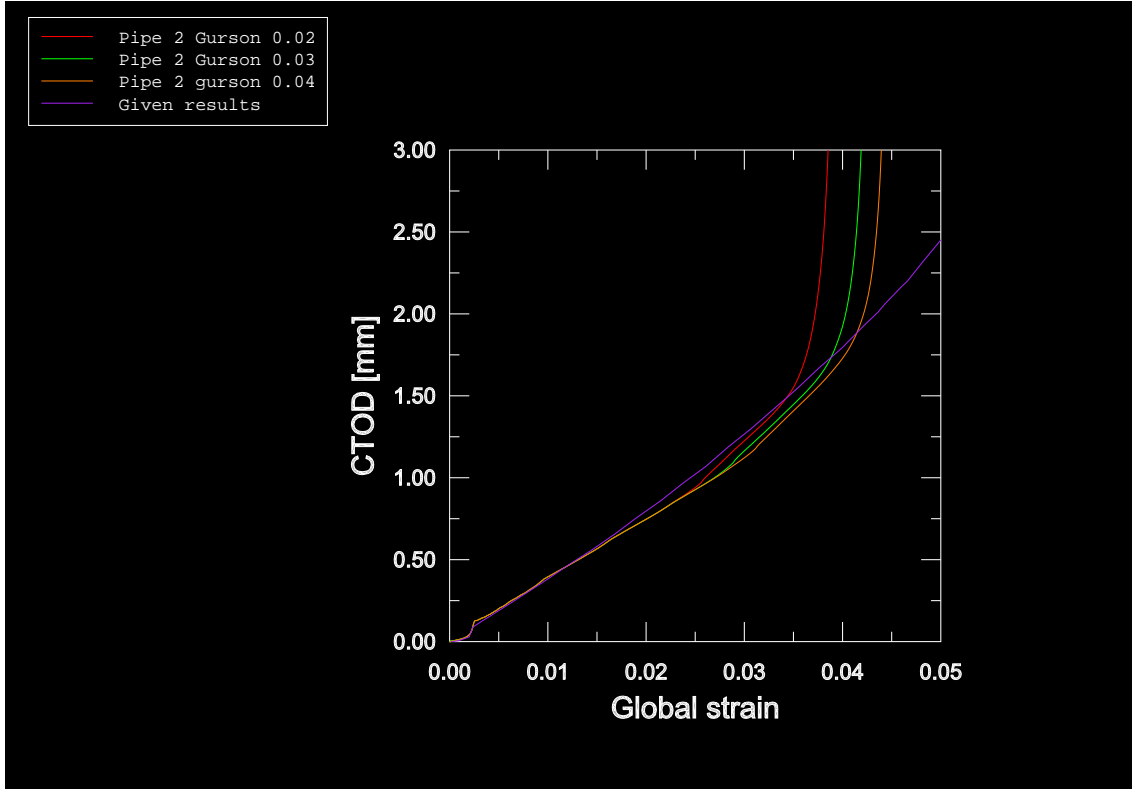
Figure 6.5: CTOD versus global strain for several critical void volume fraction

Consequently it is only useful to affect the ductile crack growth either by varying the initial void volume fraction f_0 or by modifying the critical void volume fraction f_c.

6.5   Compendium of Results of Model 2

With the refined mesh of Model 2 we were able to produce reasonable results for ductile crack growth. Ductile tearing started much earlier at a global strain of $\epsilon = 0.018$. Thus the starting point of crack growth was influenced by the finer mesh of Model 2, but not the ductile fracture behaviour itself. Also varying the Gurson parameters led only to a shunted start of crack growth.

In the next step we will determine, whether there will be any influence of the initial crack shape on the ductile fracture behaviour, since the Gurson parameter have yet no influence on it. Therefore we chose the crack length c as the parameter to vary in Model 3.

7   Model 3 – Determining the Influence of Different Initial Crack Lengths

7.1   Purpose and Model Data of Model 3

In order to get more knowledge about the influence of different initial crack lengths on the crack growth resistance, we created three similar models with different initial crack lengths. Shape and extension of all new models (named Model 3) were the same like in Model 1 and 2. Furthermore, we used the "canoe" crack shape. The initial crack depth ($a_0 = 4$ mm) remained constant whereas the crack length c was varied (overview of geometrical crack data see Figure 3.1 in Section 3.1.2).

For creating Model 3 we used a core similar to Model 2. Only two small improvements have been made: Now in Model 3 all ligament elements have the same size ($l_x = l_y = 0.25$ mm) and we realised a more fine mesh in the remaining part of the model especially next to the core. This both actions took place due to easier crack resistance measuring and they are visible in Figure A.14 in Appendix A.

We modelled the following three pipes with different initial crack extension and compared them in this step: Pipe 3–04, Pipe 3–10 and Pipe 3–30. The number at the end gives the ratio between initial crack length c and circumference U of the pipe in percent. The crack length in model Pipe 3–10 is equal to Model 1 and 2. We chose the other ratios because there are stationary results without crack growth for comparing known at SINTEF. Table 7.1 gives an overview of the crack lengths c in the particular models and the consequential total number of elements:

Model	Ratio c/U [%]	Crack length c in model [mm]	Number of elements [-]
Pipe 3–04	4	26	17781
Pipe 3–10	10	64	23811
Pipe 3–30	30	189	43969

Table 7.1: Overview of different crack lengths

We produced all models by extruding from the same core. Constant meshing for all three models in the ligament and also in the remaining part, what is the reason for the high number of elements at Pipe 3–30, should guarantee comparability between the modelled pipes.

Due to similarity to Model 2 we chose the same time period of $T = 0.1$ s and the same minimum stable time increment of $\Delta t = 1$ E - 06 s. Moreover all simulations for Model 3 were carried out by using the same Gurson parameters as for Model 1 (see Table 5.2 in Section 5.4.1).

7.2   Results

7.2.1   CTOD Results

The results of Model 3 for the values of CTOD versus global strain (see Figure 7.1) show the influence of the initial crack length. In general we can sum up that different strain levels are reached for different initial crack lengths. Although the difference in initial crack length between Pipe 3–04 and 3–10 is less in comparison to the difference between Pipe 3–10 and 3–30, the results for CTOD are vice versa. Pipe 3–10 and 3–30 tend together before the values of CTOD of Pipe 3–30 are starting to increase perceptibly for smaller global strain than of Pipe 3–10. But the results of CTOD of Pipe 3–04 are all over the time lower than the values of Pipe 3–10 and 3–30 and crack growth initiates at Pipe 3–04 at first for a much larger strain value than for the other two. This fact shows that an initial crack which covers 10% of the circumference is like a "minimum border": Pipes with longer cracks than this ratio behave nearly equal until reaching crack growth initiation. Only the crack growth itself is different due to other crack growth resistance (this is further discussed in Section 7.2.5).
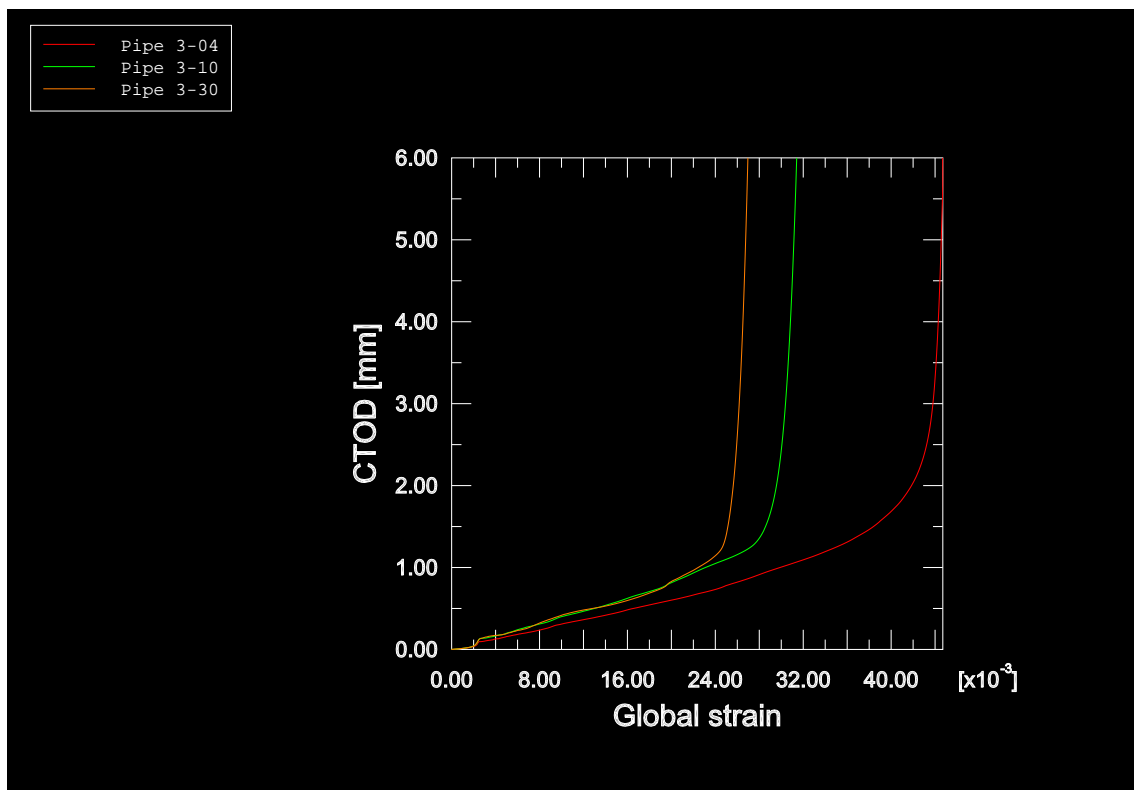
Figure 7.1: CTOD versus global strain for different initial crack lengths

7.2.2   Load Results

For the results of load versus global displacement we expected similar graphs to Model 2 with
different junctures of sudden load drop. The interesting point would be, whether there is a difference
in maximum load and what is the ratio between initial crack length c and point in time and
displacement respectively of load drop.
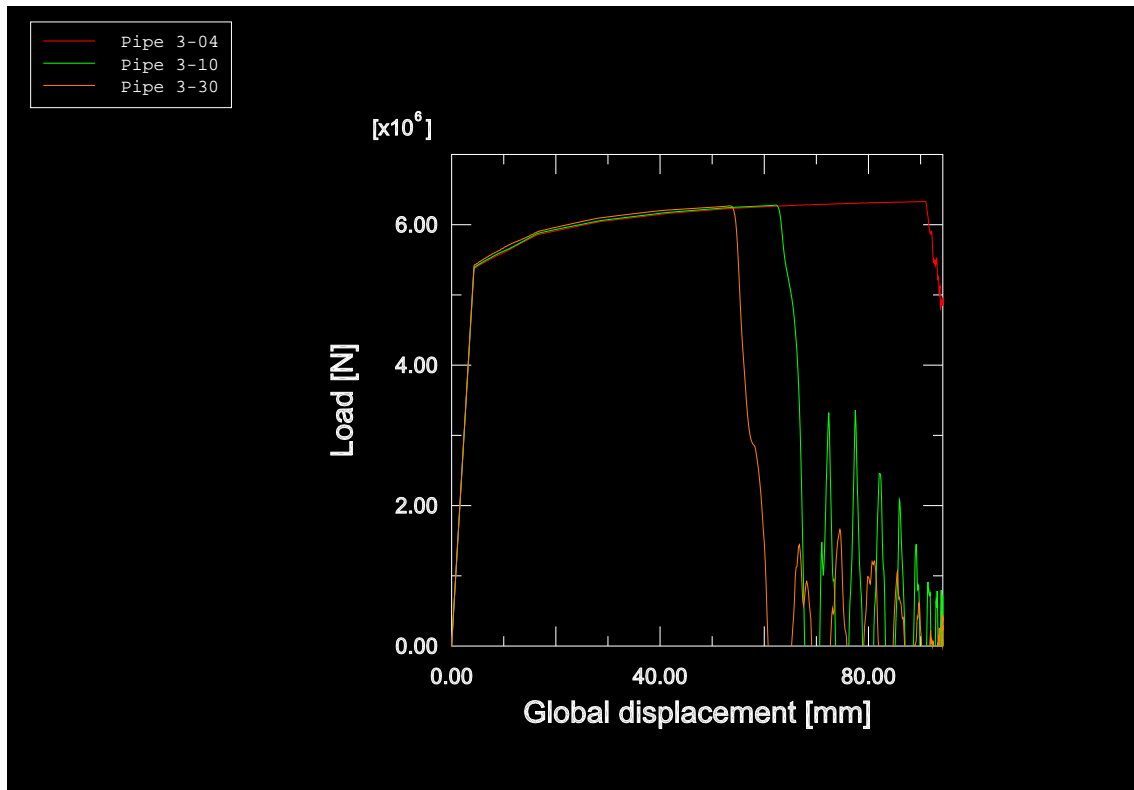
Figure 7.2: Load versus global displacement for different initial crack lengths

Figure 7.2 shows the expected load versus global displacement behaviour for the load drop. For
all initial crack lengths the carried load is almost equal until reaching the drop point. A dramatic
difference in the maximum load does not occur. Only the points in time when the load starts
to drop are comparable with the CTOD behaviour. Pipe 3–30 reaches the load drop at first and
Pipe 3–10 fails immediately after it. But for Pipe 3–04 the decrease of the load does not start until
nearly reaching the end of the analysis. Furthermore the short cracked Pipe 3–04 also does not
reach total failure, whereas the both other show the in Section 5.4.4 discussed oscillating behaviour
after decreasing to zero.

But surprisingly Pipe 3–30 has the highest load values in the beginning of the analyses, although
it contains the largest initial crack. The expected behaviour would be that the pipe with the smallest
initial crack (Pipe 3–04) is able to carry the largest amount of load. But the withershins occurred
behaviour can be explained by mass scaling. Hence Pipe 3–30 owns a much larger number of
elements and especially small ones, this model is scaled most. Table 7.2 shows as an example the

percentage change in total mass of the model at the start of the analysis:

Model	Pipe 3–04	Pipe 3–10	Pipe 3–30
Change in total mass [%]	305	433	850

Table 7.2: Percentage change in total mass at Model 3

Although all three models have the same minimum stable time increment of $\Delta t = 1\,\mathrm{E}\text{-}06\,\mathrm{s}$, the change in total mass is strongly divergent due to a different number of relative small elements. Thus the results of Pipe 3–30 are much more influenced by mass scaling than the other two. Combining the results from Figure 7.2 with the knowledge of the load behaviour at different mass scaling from Figure 5.5 in Section 5.3.2 the received values are consequential. Since we applied global displacement as a smooth function in ABAQUS Explicit (see Section 2.4.3) the increase of load shrinks by nearly reaching the end of the total time period ($T = 0.1\,s$). So this load increase is too little in order to reach total loss of load carrying capacity or total pipe failure respectively at Pipe 3–04.

7.2.3   Crack Growth Δa for Different Initial Crack Lengths

A more precise examination of the crack growth behaviour for different crack lengths should give better understanding of the crack growth behaviour until reaching total failure. Therefore we measured manually the values of crack growth Δa like described in Section 4.2.5.

For comparing with and verifying LINKpipe[2] results it was necessary to redefine crack growth now by reaching critical void volume fraction f_c instead of the void volume fraction of final failure f_F. So we changed the output to void volume fraction (VVF) instead of the STATUS output for measuring crack growth.

A visual comparison of the crack growth for the different models is given by the three Picture Sequences 2,3 and 4 in Appendix C,D and E. There the elements, which already reached the critical void volume fraction f_c, are plotted in orange colour. At first we can summarise that the crack growth is to some extend equal for all pipes. The cracks grow among maintaining their "canoe" shape and the absolute amount of circumferential crack growth until through crack happens is the same. Furthermore, we can determine that crack growth starts next to the x-y-plane at the short and intermediate cracked pipes (see Picture Sequence 1 for Pipe 3–04 and Picture Sequence 2 for Pipe 3–10, both in Appendix).

Whereas viewing the long cracked model Pipe 3–30 (see Picture Sequence 3 in Appendix E) we can experience that crack growth does not start in the element next to the x-y-plane as for the

---

[2]LINKpipe is a fracture mechanics software tool produced in collaboration between SINTEF and NTNU in Trondheim.

other models. It starts in the middle of the modelled crack and extends first to both circumferential directions before finally the "canoe" shaped crack grows towards the pipe center.

Former results from SINTEF according to Østby [9] which are schematically displayed in Figure 7.3 also indicate a connected issue to that crack growth behaviour in Pipe 3–30.
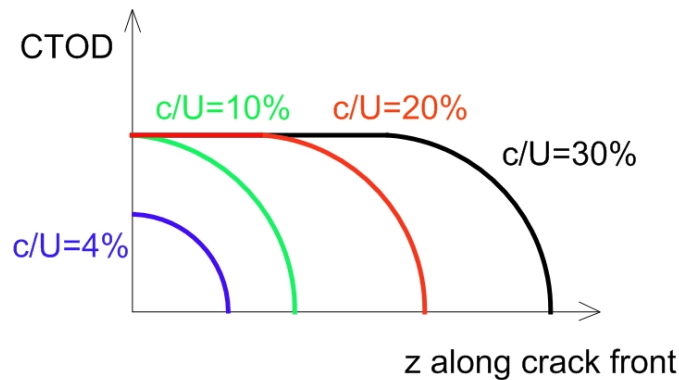
Figure 7.3: CTOD along crack front for different ratios c/U according to Østby [9]

For cracks with a ratio c/U larger than 10 % CTOD is constant for a certain extension along the crack length (circumferential direction) at an arbitrarily point in time. Pipes with a ratio of $c/U = 0.1$ are like a "minimum border" as explained in Section 7.2.1. For pipes with a lower ratio c/U than 10 % only smaller values of CTOD are reached at the same moment.
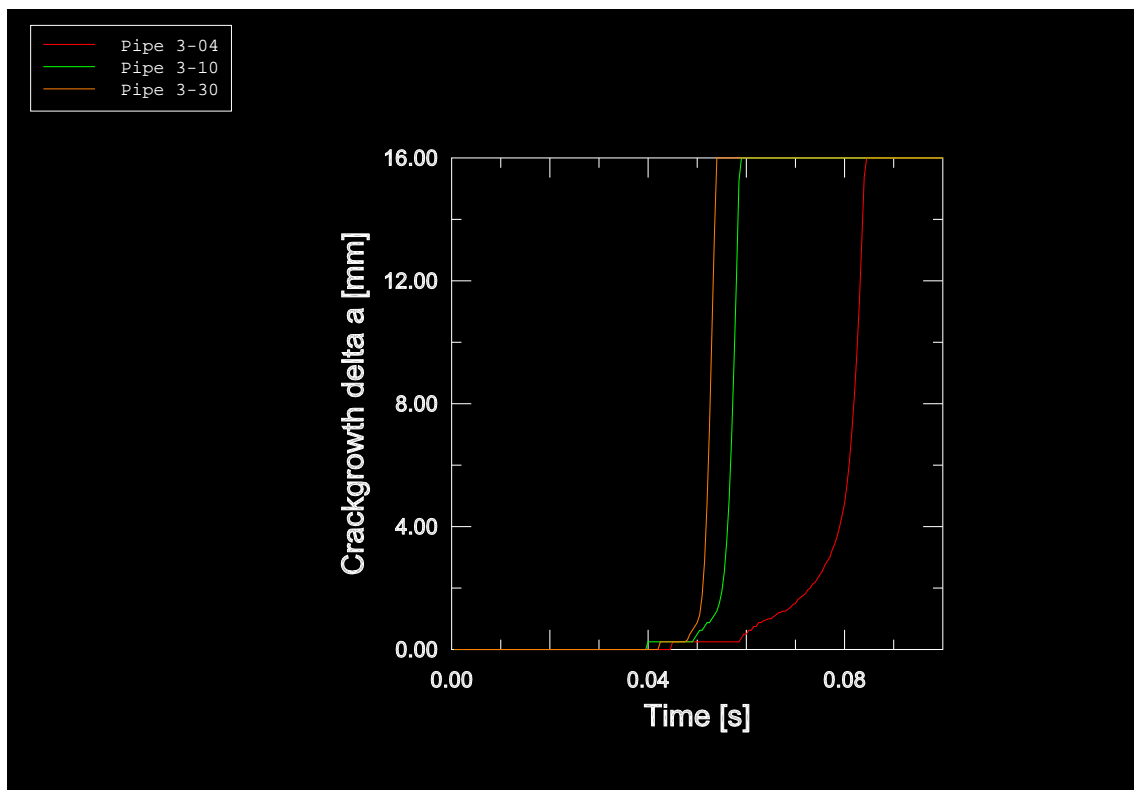
Figure 7.4: Crack growth versus time for different initial crack lengths

Figure 7.4 shows the re-imported results of the crack growth Δa. We gained that data from results plotted in a similar style to them in Appendix C,D and E. It can be seen in Figure 7.4 that crack growth initiates for all three models nearly at the same point in time. By viewing exactly it is visible that crack growth starts at first at Pipe 3–10, then at 3–30 and finally at Pipe 3–04. This somewhat strange order is affected by the measuring method (see Section 4.2.5), where Δa is recorded at $z = 0$. After initiation the crack growth remains for a certain time constant, where the duration of that stability is dependent on the initial crack length. The area of remaining cross section material at the beginning of the analysis is the equivalent of the initial crack length. Thus the less initial crack cross section area, the longer crack growing stability, what is especially obvious at Pipe 3–04.

The gradient of increase of Δa up to through-crack ($\Delta a = 16\ mm$) is relatively identical for Pipe 3–10 and 3–30. At Pipe 3–04 this rise is smaller due to more intact remaining cross section area at the crack plane. Furthermore, this slower crack growth behaviour is also influenced by applying less load by the smooth shape of the load amplitude. But all cognitions are time dependent and therefore statements about crack growth resistance can not be made here (see Section 7.2.5).

7.2.4   Load Drop Process

In order to get a better understanding of the load drop process we combined the data of load and crack growth versus time:
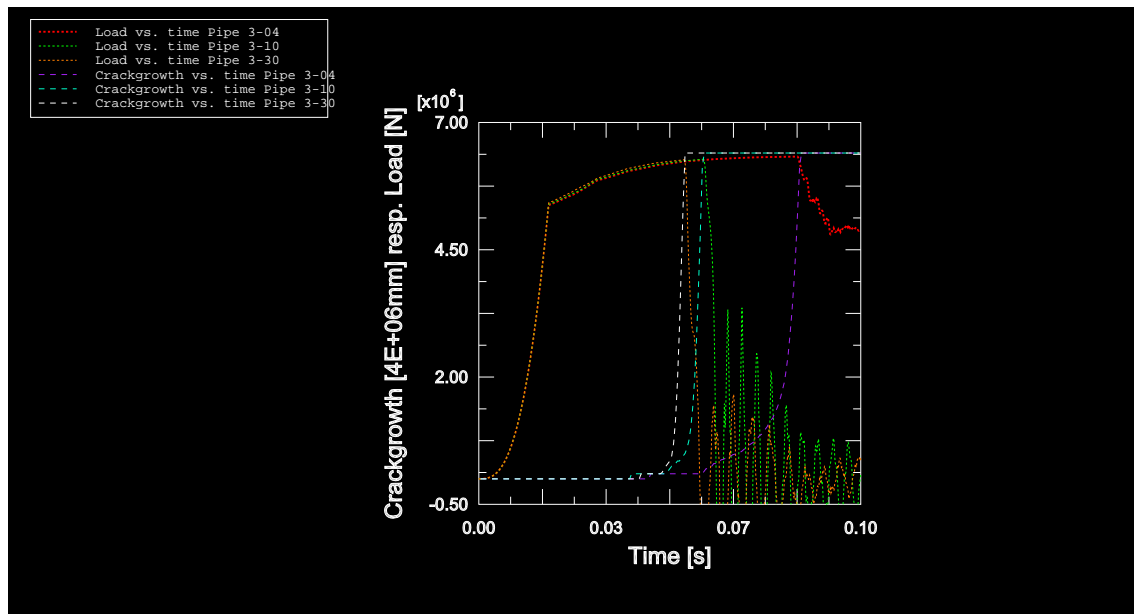
Figure 7.5: Load versus time combined with crack growth versus time for different crack lengths

Owing to easier visibility the crack growth Δa in Figure 7.5 is scaled with a factor of $s = 4\text{E}+05$. So crack growth has started after leaving the lower plateau ($\Delta a = 0$) and through crack takes place

by reaching the upper plateau ($\Delta a = s \cdot 16\,\text{mm} = 4\,\text{E}+05 \cdot 16\,\text{mm} = 6.4\,\text{E}+06\,\text{mm}$). The oscillating part of the load results of the short and the intermediate crack after load drop should be neglected.

We can determine that the sudden drop in load occurs at the same point in time with through crack for all three models. But we can not experience an influence of the growing crack on the load progression before the load drops. Total failure of the pipe, that is when a load carrying capacity of zero is reached, takes always place a certain time after through crack has happened. But the duration (both in time and load) between crack growth initiation and final failure is small at Pipe 3–10 and 3–30. Only at Pipe 3–04 it takes a longer time between these two events. This is caused by more intact cross section material at the beginning of the analysis but also influenced by the applied smooth amplitude.

7.2.5   Crack Growth Resistance for Different Initial Crack Lengths

As the last point in this project the crack growth resistance for all three cases should be examined[3]. Therefore the results of CTOD and crack growth versus time were combined. This should provide a time independent statement of crack growth resistance.
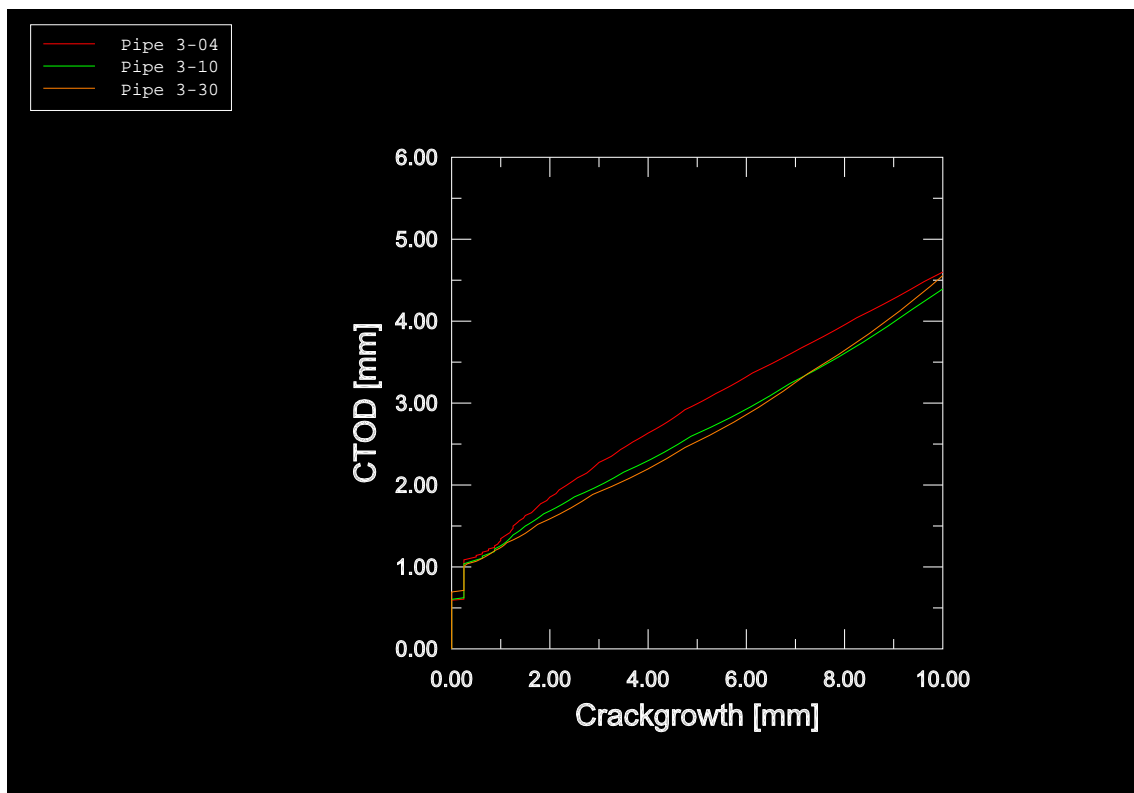
Figure 7.6: CTOD versus crack growth for different initial crack lengths

---

[3]We analysed crack growth resistance for all models, since the values are needed as material input for future simulations in LINKpipe.

Figure 7.6 shows the crack growth resistance behaviour only until crack growth is reaching $\Delta a = 10$ mm. We focused only on the start region of the analysis since this is most relevant for crack resistance. A vital difference between Pipe 3–10 and Pipe 3–30 can not be determined and Pipe 3–04 also tends to the same shape. The crack growth resistance for the shortest crack is of course higher than for the other two. At all three models crack growth initiates at a CTOD level of around $\delta = 0.7$ mm. That quite large value is caused by the still relative large element size of $l = 0.25$ mm in the ligament and could be refined in future work. Although the results for Pipe 3–04 trend to descend after $\Delta a = 4$ mm whereas the CTOD values of the other two models seem to ascend, it can be said that there is only a small influence of the initial crack length c on the crack growth resistance of pipes with small surface crack with a ratio of $c/U < 10\%$. But the initial crack length has almost no influence on the CTOD value at crack initiation.

7.3   Compendium of Results of Model 3

Testing the influence of the initial crack length c on ductile fracture behaviour with three comparable models showed that ductile tearing starts at all initial crack lengths at the same point in load. Different strain levels were reached at final pipe failure, whereas the maximum load was almost equal. The results also displayed that a pipe with an initial crack with a ratio of $c/U < 10\%$ has a higher crack growth resistance than one with a larger initial crack. For pipes with initial cracks with a larger ratio than $c/U = 10\%$ the crack growth resistance is not any more appreciably influenced. But we obtained all these results by holding the initial crack depth constant. So further investigations into simulations with a varied initial crack depth would be useful.

8 Fracture Mechanics Assessment and Discussion

In this project we have investigated the influence of several issues on ductile fracture behaviour:

In order to be able to evaluate the reliability of the results we have studied the influence of load rating and mass scaling on the quality of the results. It has turned out that the results can only be diminished in quality by these procedures.

Furthermore, we have examined the influence of the Gurson parameters on ductile fracture behaviour. We have found out that only the point in time and load respectively can be influenced by changing the values of the Gurson parameters. However, the ductile fracture behaviour itself is not affected by these parameters.

Moreover, we have analysed the influence of the mesh size on ductile fracture behaviour. Refining the element size in the crack tip region will, as expected, result in a more reasonable earlier onset of ductile tearing. The response of the load drop behaviour also improves by using constant small elements all over the ligament.

As regards final pipe failure it has been found that a different initial crack length results in different strain levels whereas the maximum load is indifferent to the initial crack length. Thus failure criteria for pipe fracture should be strain based instead of maximum load based. Finally, we have ascertained that the crack growth resistance of pipes only depends on the initial crack length as long as this is less than 10 % of the circumference.

Results for different initial crack lengths must always be considered with respect to the constant crack depth in all cases. We conclude that further investigations regarding the influence of the initial crack depth on ductile fracture behaviour is essential.

9   Summary and Future Work

In this project we have successfully simulated ductile fracture behaviour of pipe sections with surface crack using ABAQUS Explicit software. After determining the influences of load rating and mass scaling, we have implemented the Gurson routine in order to obtain ductile tearing. We have found that the onset of ductile tearing is dependent on the mesh size in the crack tip region, whereas the crack growth behaviour itself is indifferent to the mesh size. Furthermore, we have studied the influence of the Gurson parameters: Varying the Gurson parameters influences only the point in time and load respectively of the onset of crack growth and not the crack growth behaviour itself, once it is initiated. Finally, we have examined the influence of the initial crack length on ductile fracture behaviour. We have found that the initial crack length influences the level of strain at final failure, whereas the maximum load is indifferent to the initial crack length. Furthermore, we have detected that the crack growth resistance is only affected if the initial crack is shorter than 10 % of the circumference.

The following items could be considered for future work in order to obtain further knowledge about ductile fracture behaviour of pipes with surface crack:

- The pipe could be loaded in bending case, since this is the important load case in real offshore use of pipes.

- The initial crack depth could be varied under holding the crack length constant in order to determine its influence.

- The material hardening behaviour could be changed by modifying the strain hardening exponent n.

- Internal pressure could be applied as a additional boundary condition in order to simulate more realistic conditions.

References

[1] Anderson TL, "Fracture Mechanics - Fundamentals and Applications; Second Edition", CRC Press Inc., Boca Raton, 1995.

[2] Zhang ZL, Handouts of lecture "Fracture mechanics", NTNU Trondheim, 2004

[3] ABAQUS, Version 6.4., Hibbit, Karlsson and Sorensen (HKS) Inc., 2003.

[4] Chen Y and Lambert S, "Finite Element Modeling of ductile tearing of pipeline-steel in cracked plates", International Pipeline Conference, Calgary, 2004.

[5] Gurson AL, "Continuum theory of ductile rupture by void nucleation and growth: Part I - Yield criteria and flow rules for porous ductile materials", Journal of Engineering Materials and Technology, Vol. 99, pp. 2-15, 1977.

[6] Tvergaard V, "Influence of voids on shear band instabilities under plane strain conditions", International Journal of Fracture, Vol. 17, pp. 389-407, 1981.

[7] Zhang ZL, "A complete Gurson model", SINTEF Materials technology, Trondheim

[8] Zhang ZL, Hauge M and Thaulow C, "Two parameter characterization of the near-tip stress fields for a bi-material elastic-plastic interface crack", International Journal of Fracture, Vol. 79, pp. 65-83, 1996.

[9] Østby E, written and oral remarks, SINTEF Materials and Chemistry, Trondheim, 2004

[10] Eriksson M, written and oral remarks, SINTEF Materials and Chemistry, Trondheim, 2004

Appendix

A Figure A.1–A.14
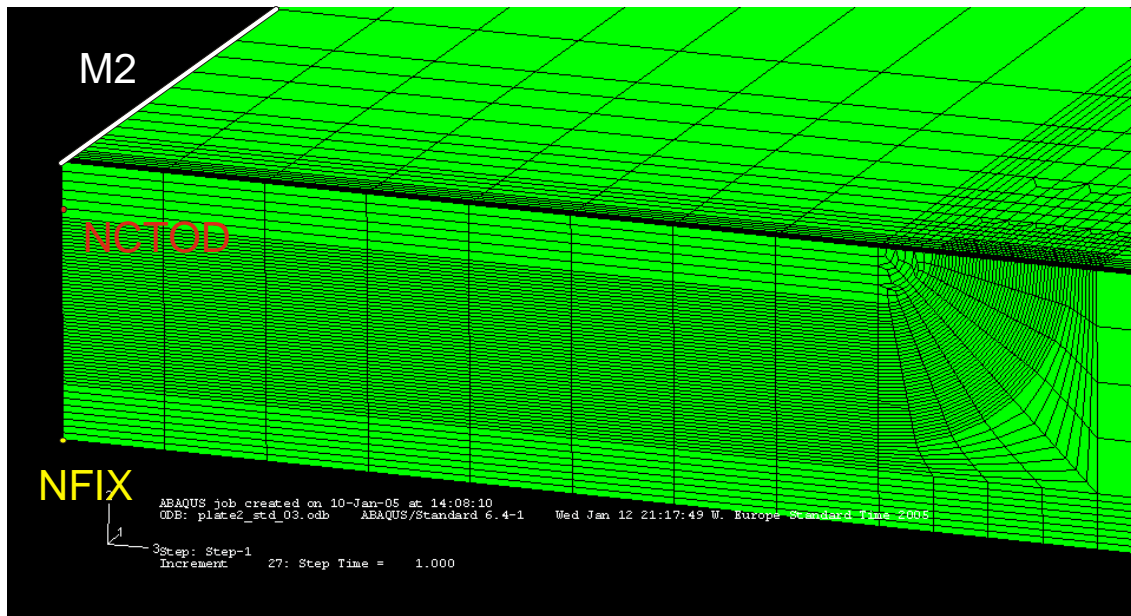
Figure A.1: Overview of groups – 1
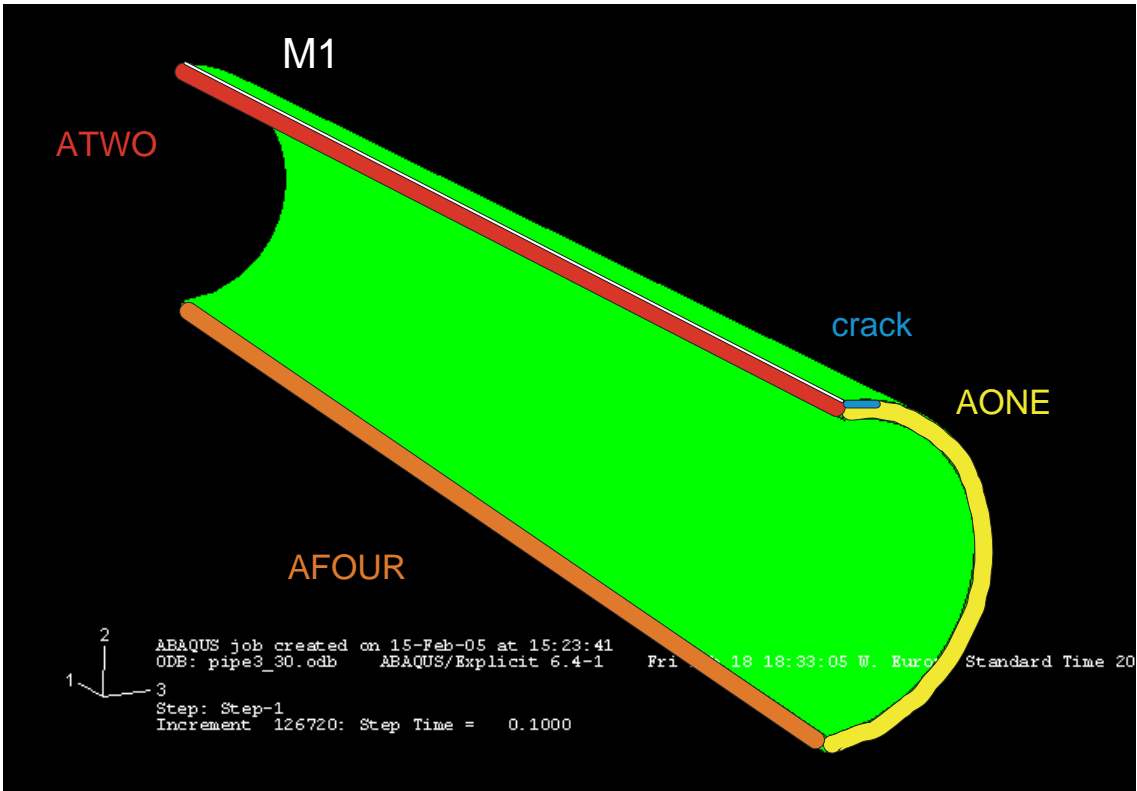
Figure A.2: Overview of groups – 2
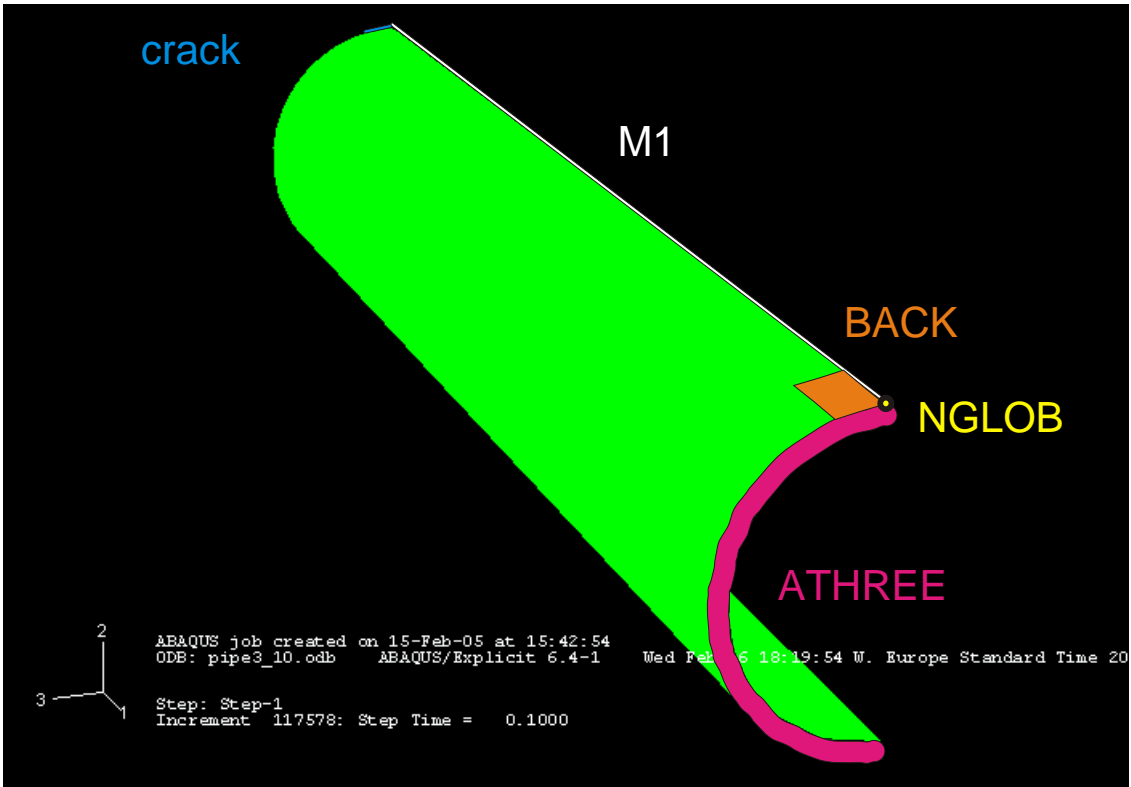
Figure A.3: Overview of groups – 3
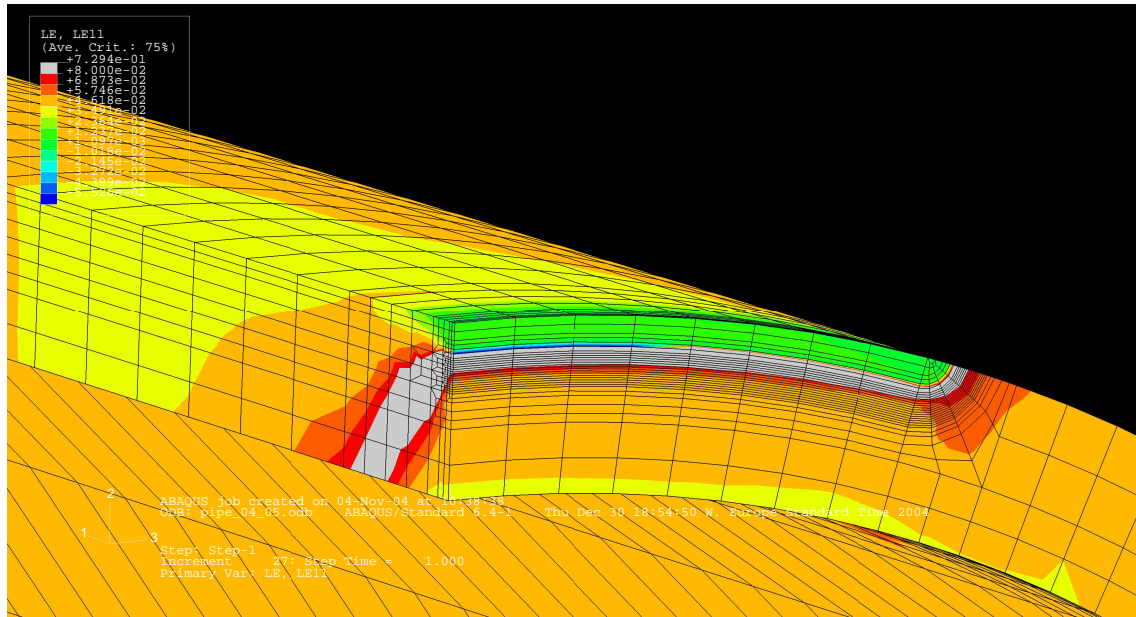
Figure A.4: Strain dispersal near the cracktip for Pipe 1 run in ABAQUS Standard
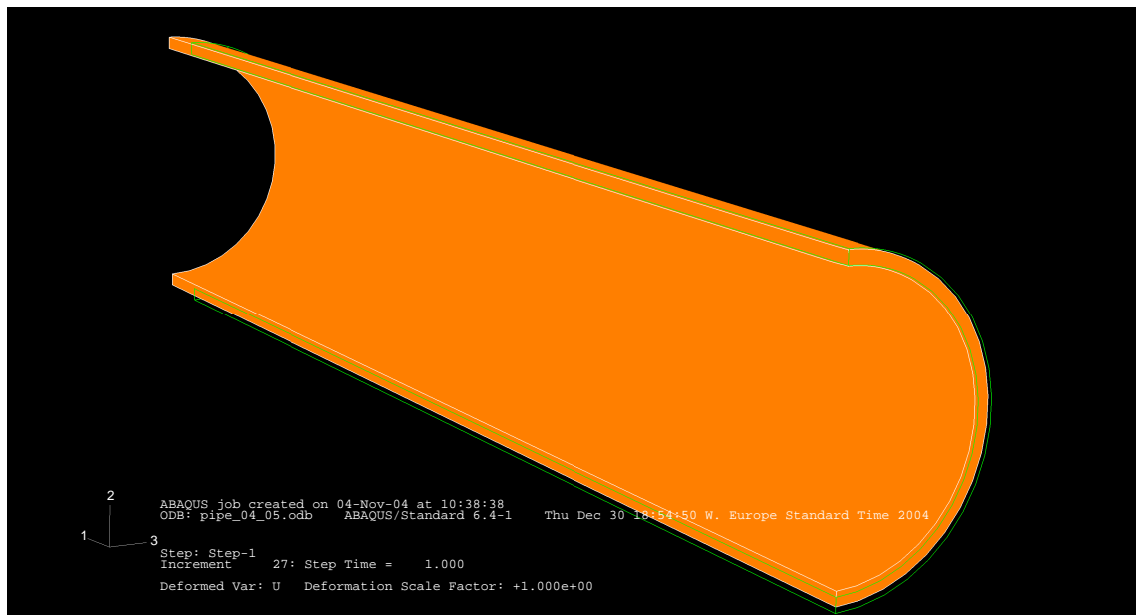
Figure A.5: Superimposing undeformed (green) and deformed shape (white filled with orange)
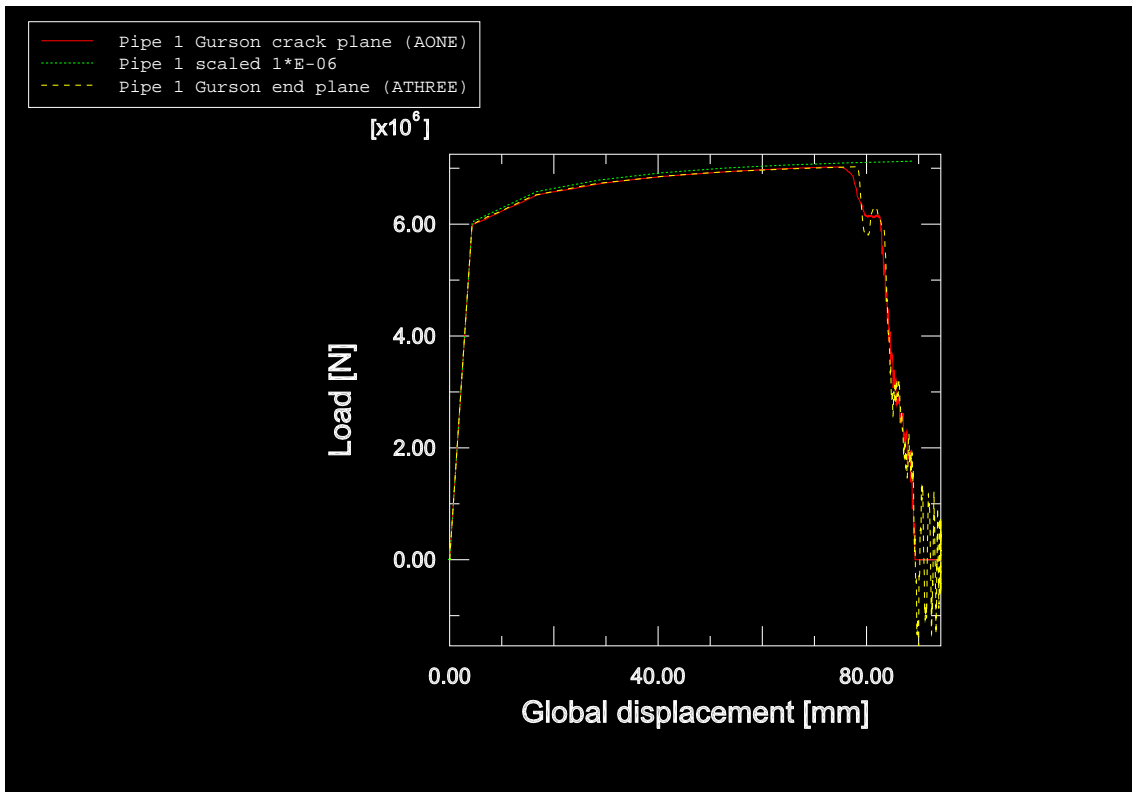
Figure A.6: Load versus global displacement for Pipe 1 with implemented Gurson material
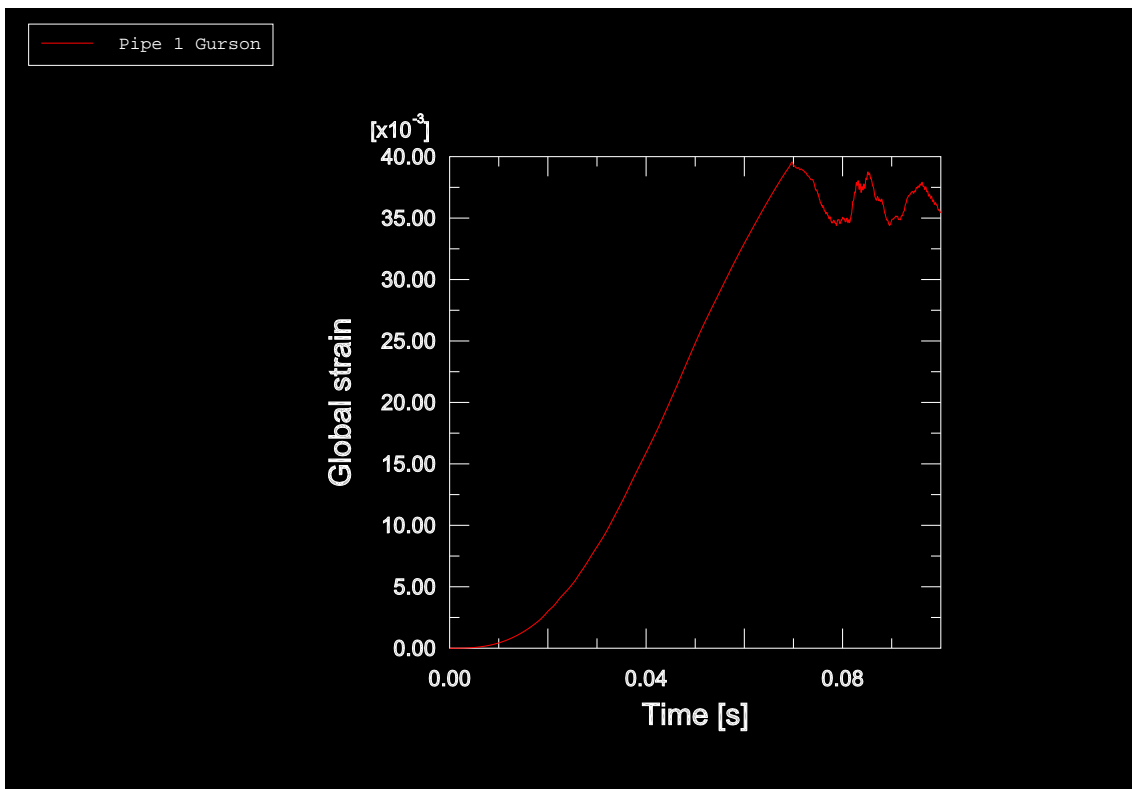
Figure A.7: Global strain versus time for Pipe 1 with implemented Gurson material
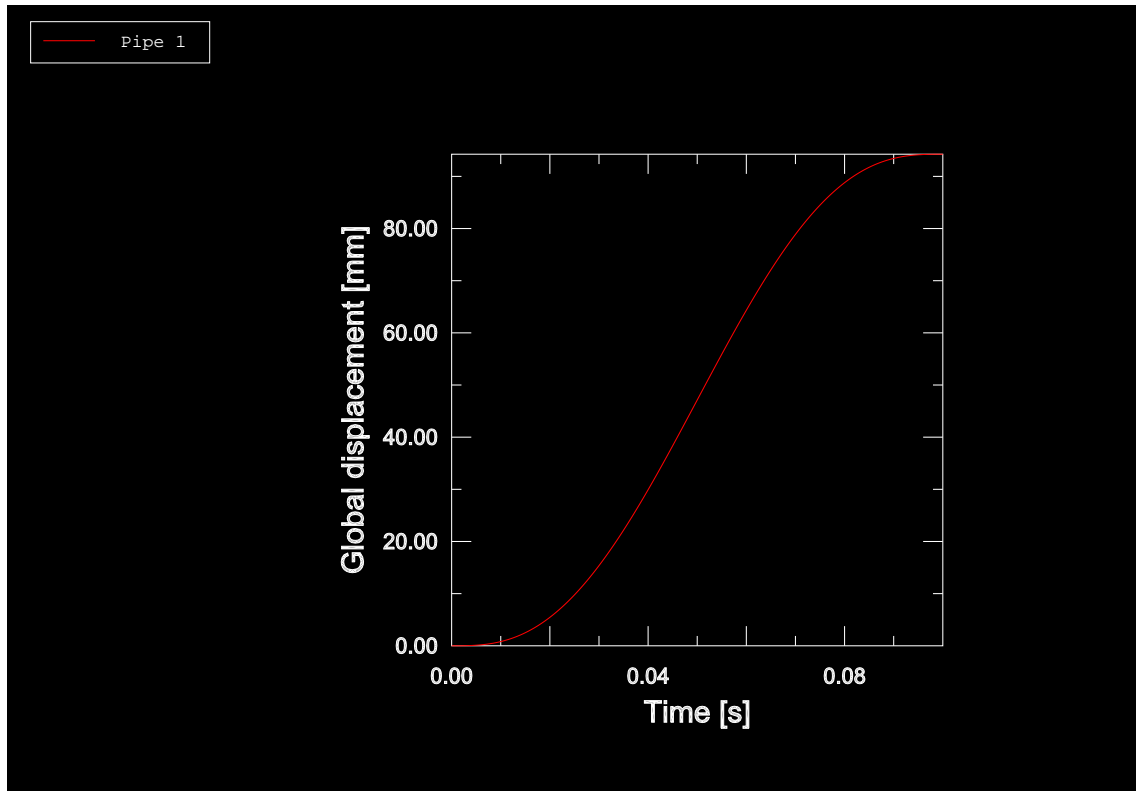
Figure A.8: Global displacement versus time (applied smooth amplitude) for Pipe 1 with implemented Gurson material
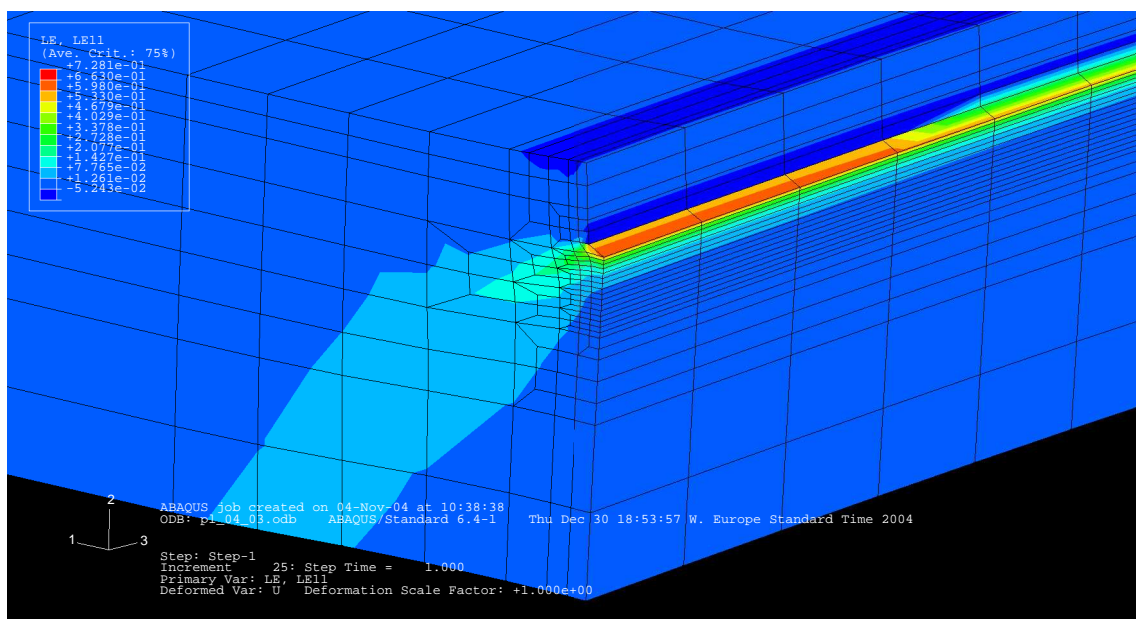
Figure A.9: Global strain behavior near the crack tip for Plate 1
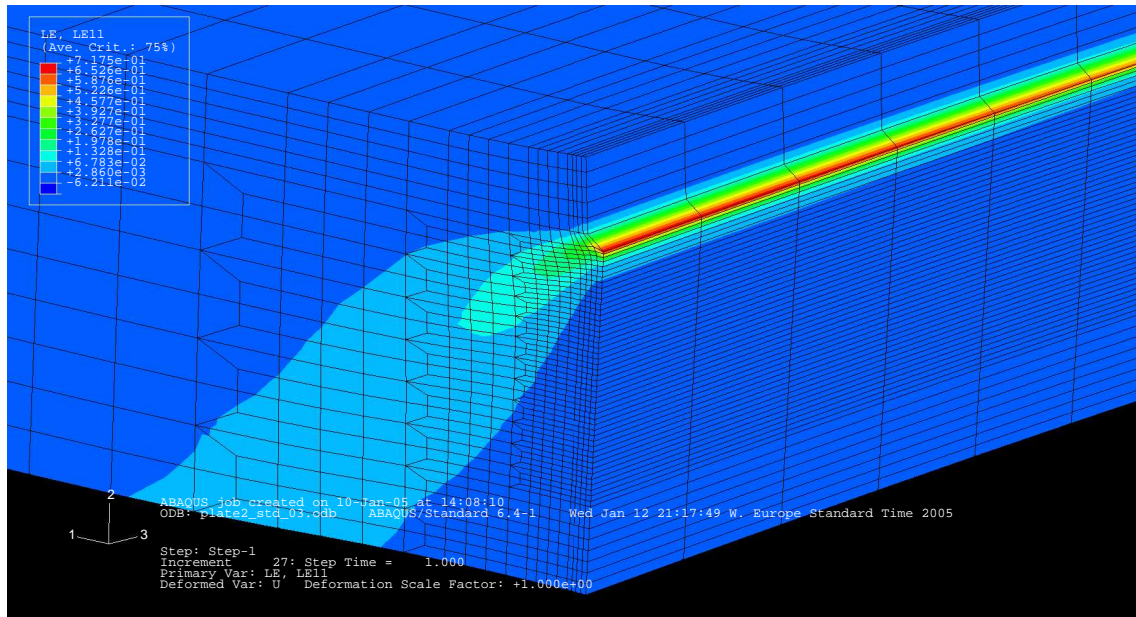
Figure A.10: Global strain behavior near the crack tip for Plate 2
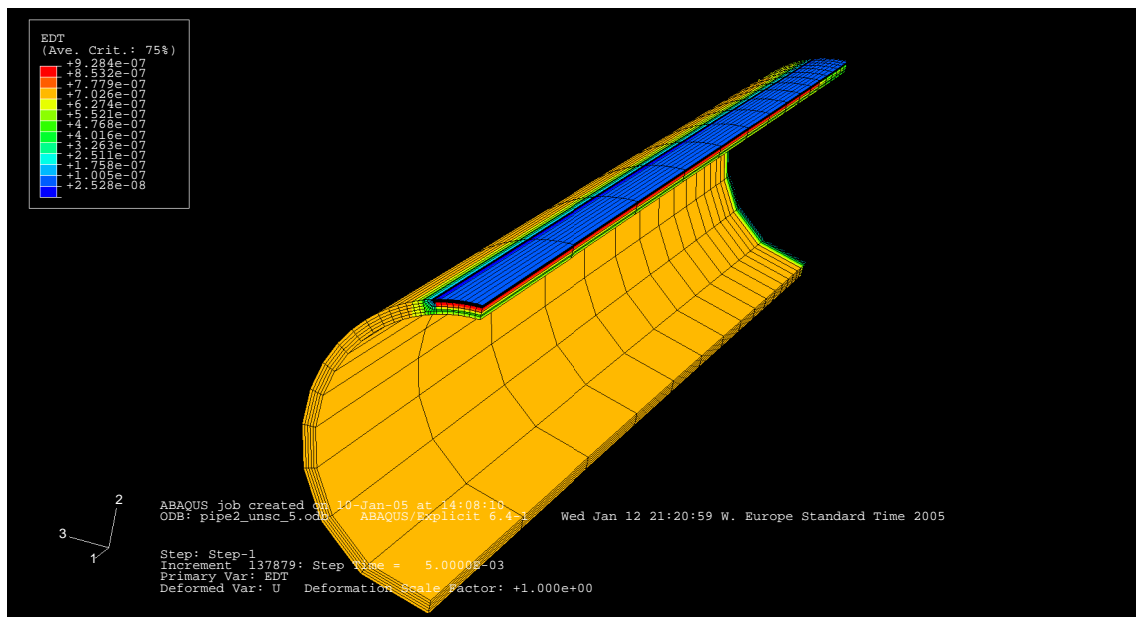
Figure A.11: Stable time increments for all elements in Model 2
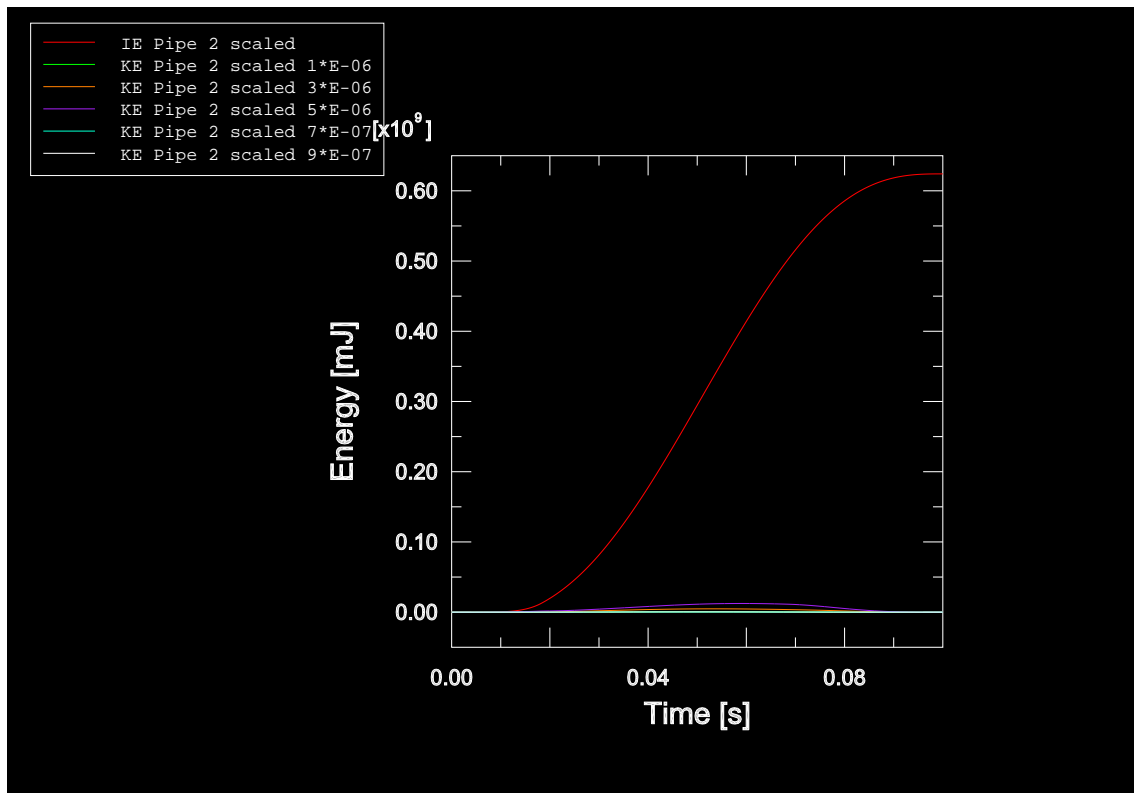
Figure A.12: Comparing internal ("IE") and kinetic energy ("KE") of Model 2 for several mass scaling
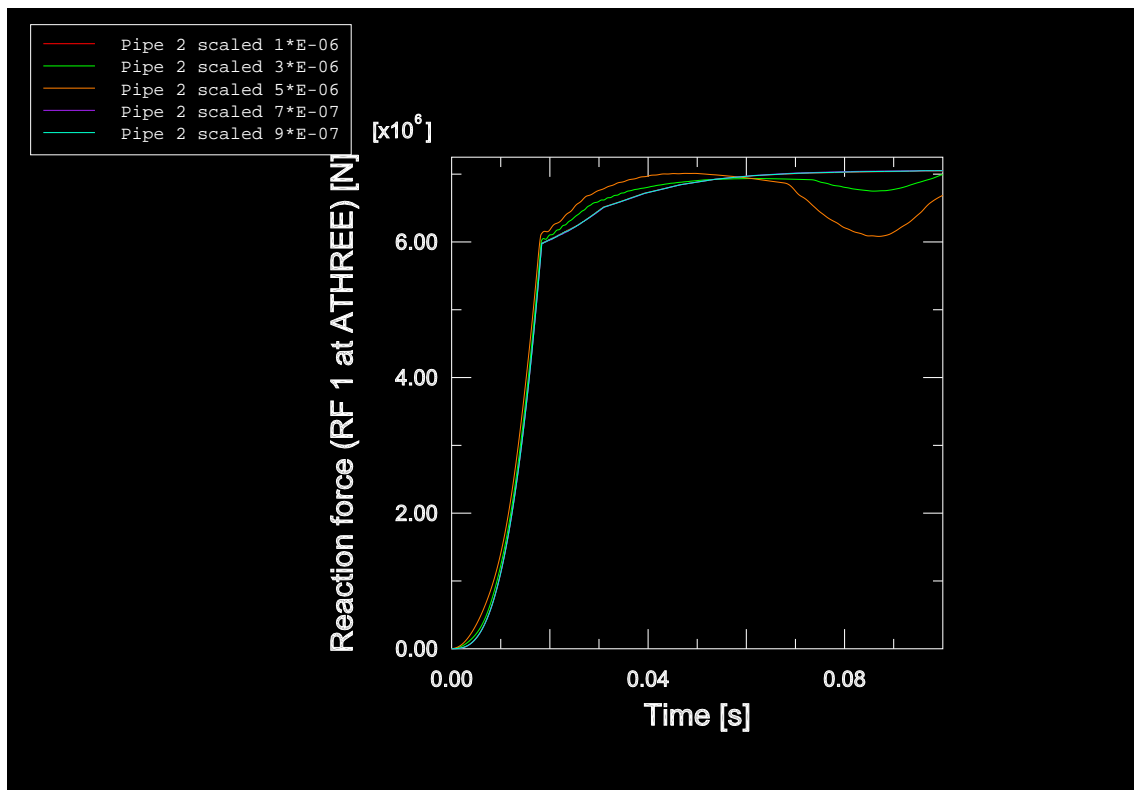
Figure A.13: Comparing reaction forces of Model 2 for several mass scaling

57
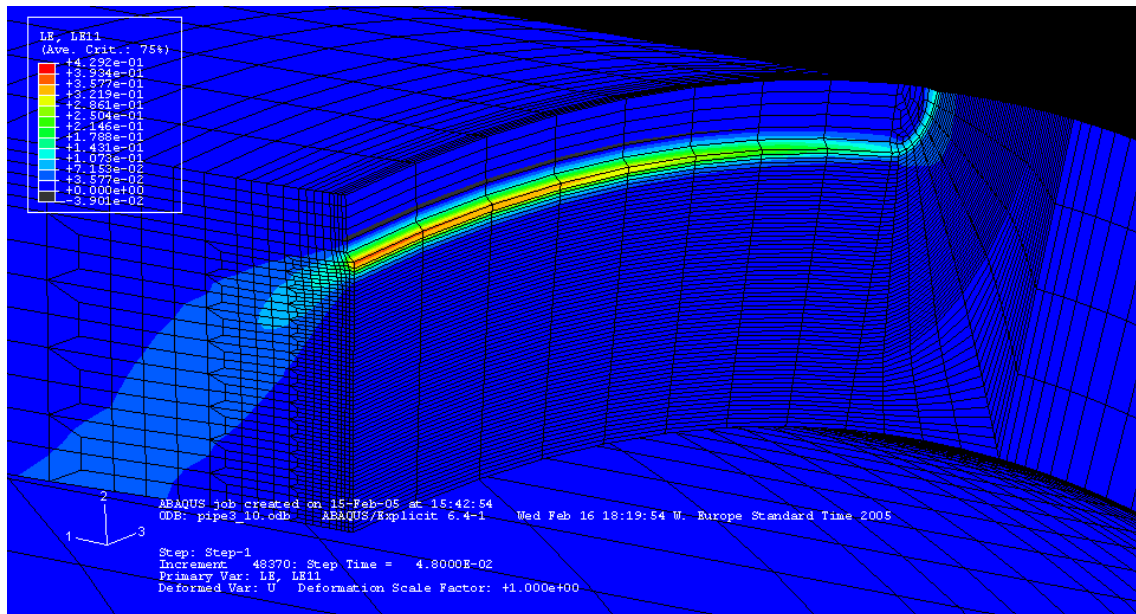
Figure A.14: Overwiew of mesh of Model 3

B Picture Sequence 1: Crack Growth of Pipe 1
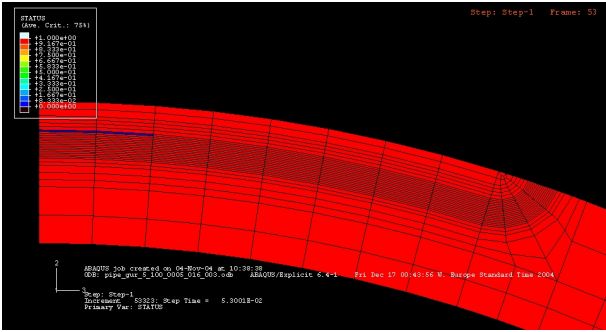
Figure B.1: $\tau = 0.0530$ s
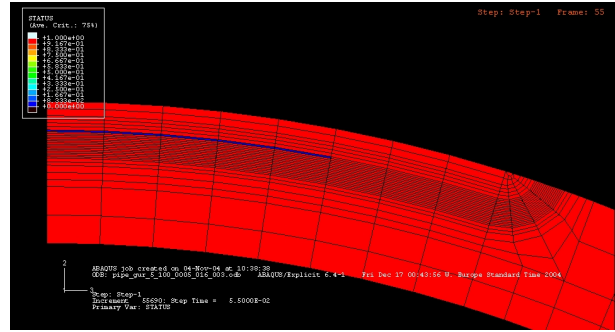
Figure B.2: $\tau = 0.0550$ s
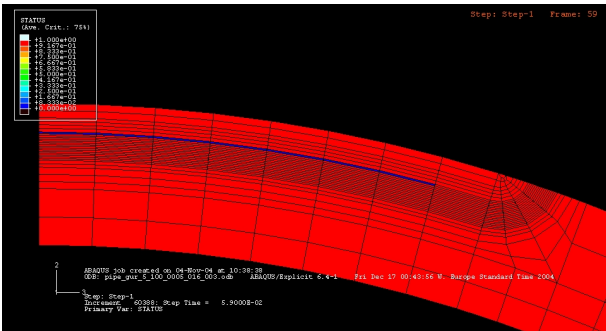
Figure B.3: $\tau = 0.0590$ s
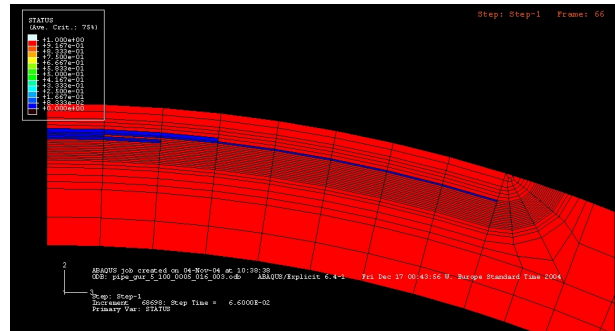
Figure B.4: $\tau = 0.0660$ s
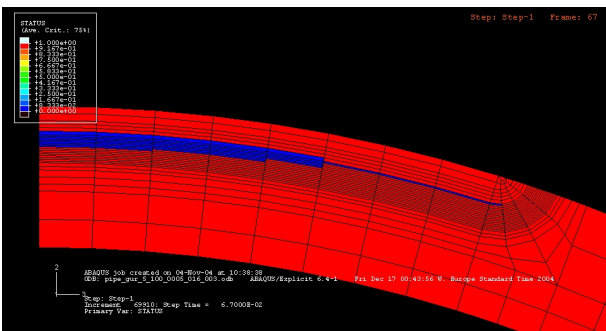
Figure B.5: $\tau = 0.0670$ s
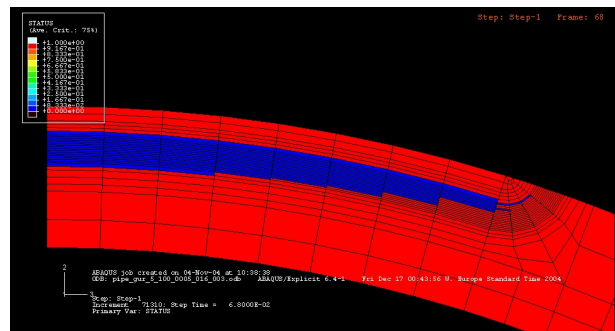
Figure B.6: $\tau = 0.0680$ s
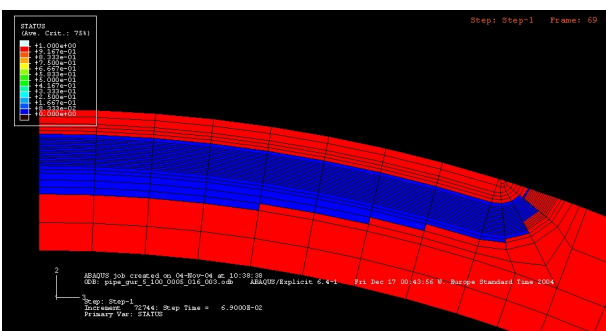
Figure B.7: $\tau = 0.0690$ s
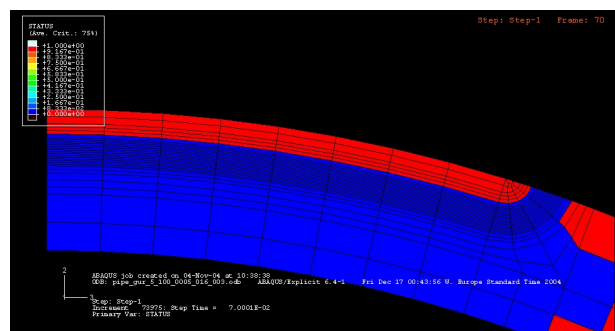
Figure B.8: $\tau = 0.0700$ s

C Picture Sequence 2: Crack Growth of Pipe 3–04
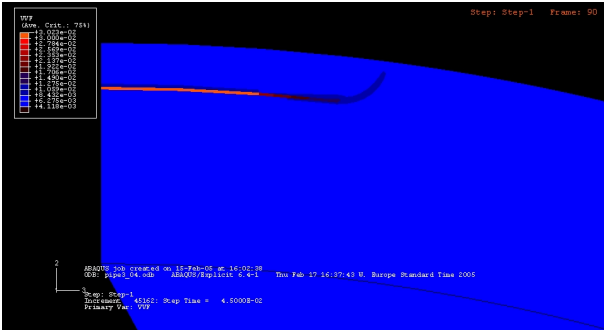
Figure C.1: $\tau = 0.0450$ s
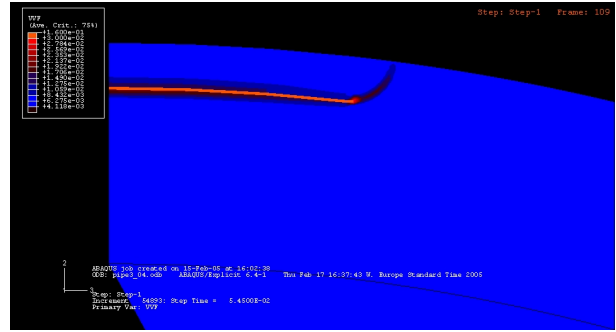
Figure C.2: $\tau = 0.0545$ s
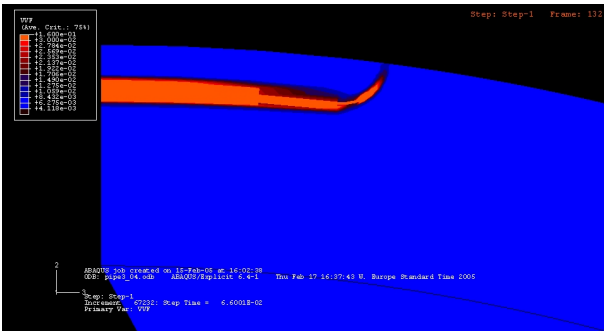
Figure C.3: $\tau = 0.0660$ s
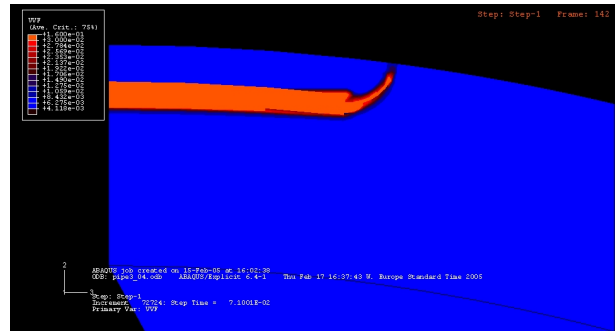
Figure C.4: $\tau = 0.0710$ s
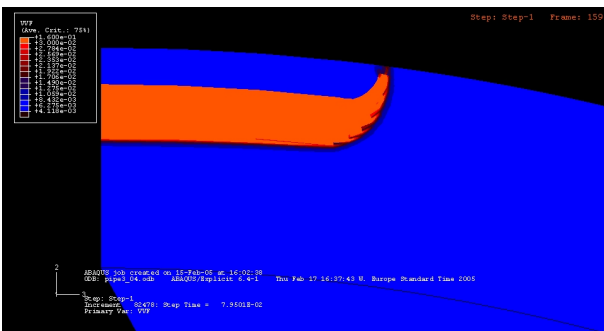
Figure C.5: $\tau = 0.0795$ s
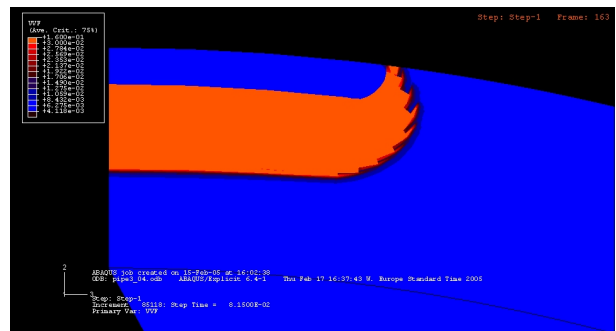
Figure C.6: $\tau = 0.0815$ s
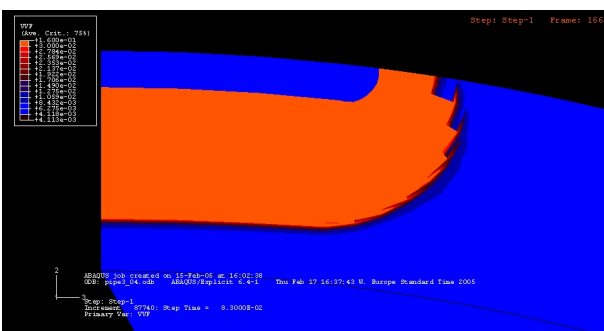
Figure C.7: $\tau = 0.0830$ s
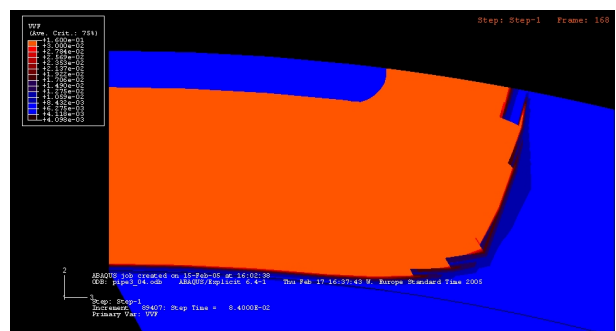
Figure C.8: $\tau = 0.0840$ s

D Picture Sequence 3: Crack Growth of Pipe 3–10
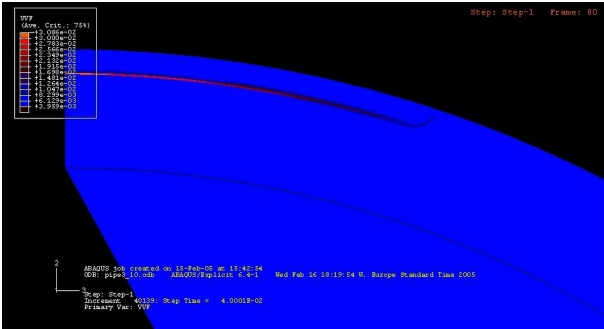
Figure D.1: $\tau = 0.0400$ s
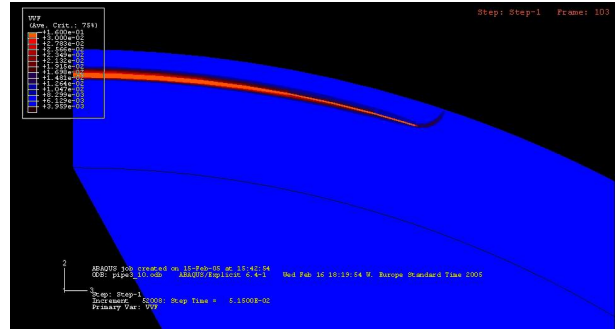
Figure D.2: $\tau = 0.0515$ s
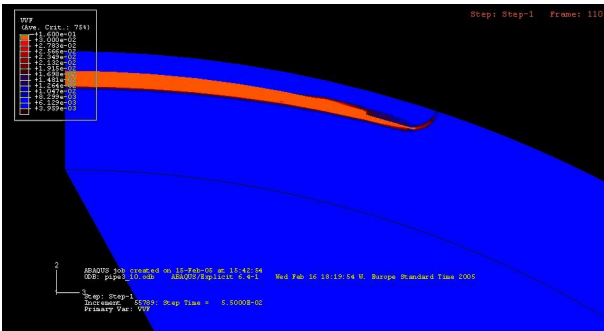
Figure D.3: $\tau = 0.0550$ s
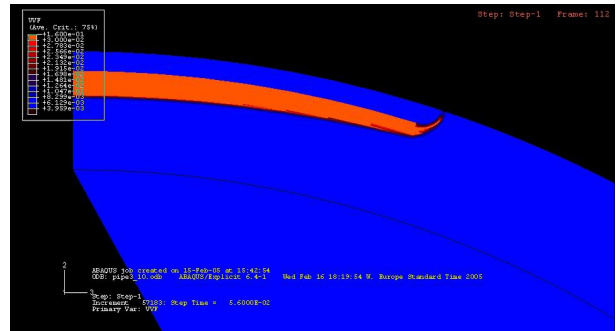
Figure D.4: $\tau = 0.0560$ s
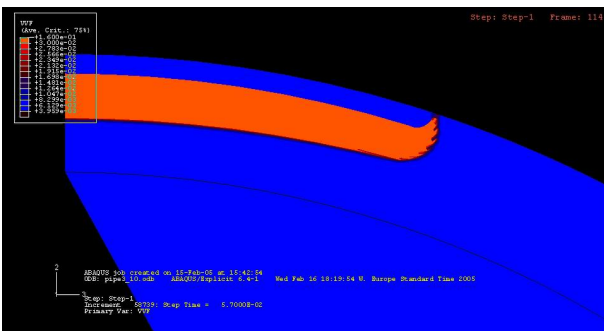
Figure D.5: $\tau = 0.0570$ s
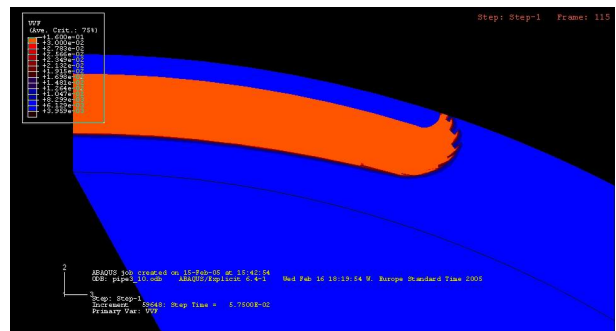
Figure D.6: $\tau = 0.0575$ s
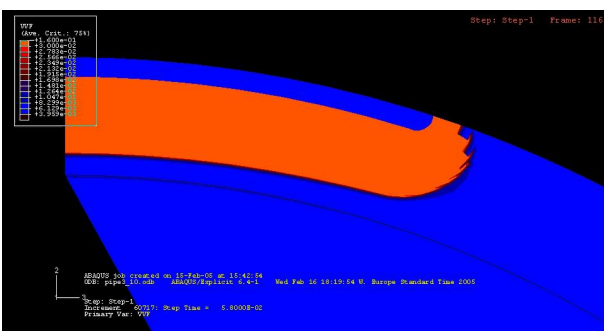
Figure D.7: $\tau = 0.0580$ s
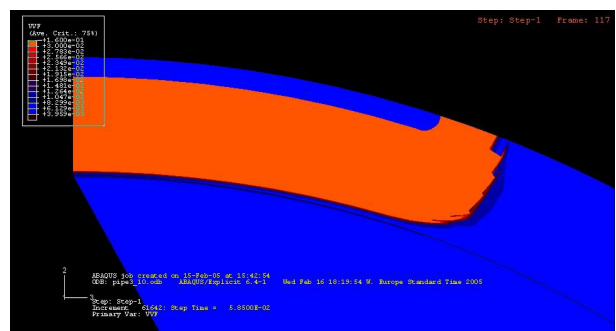
Figure D.8: $\tau = 0.0585$ s

E Picture Sequence 4: Crack Growth of Pipe 3–30
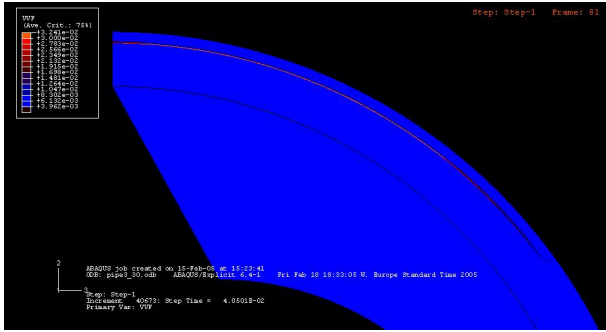
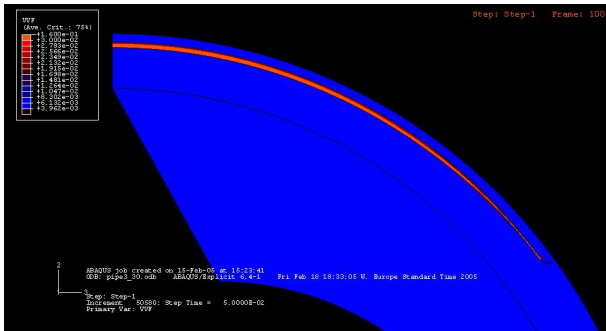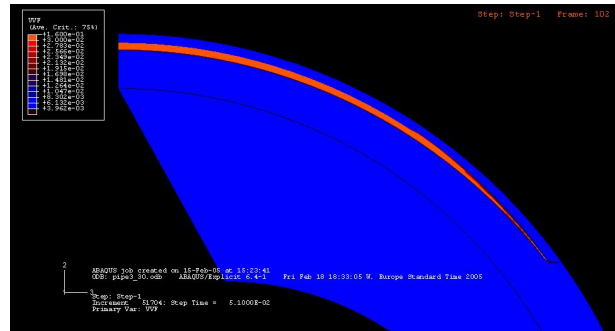Figure E.1: $\tau = 0.0405$ s
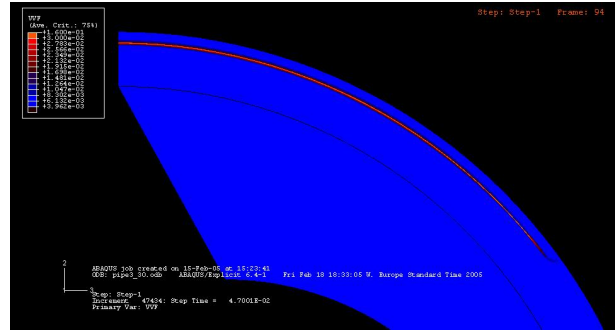
Figure E.2: $\tau = 0.0470$ s

Figure E.3: $\tau = 0.0500$ s

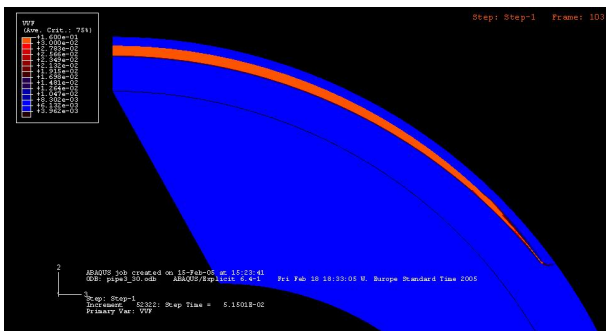Figure E.4: $\tau = 0.0510$ s

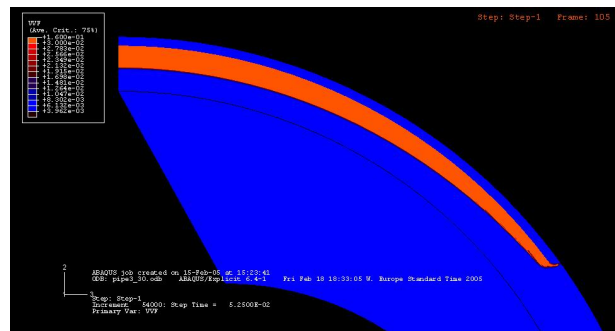
Figure E.5: $\tau = 0.0515$ s
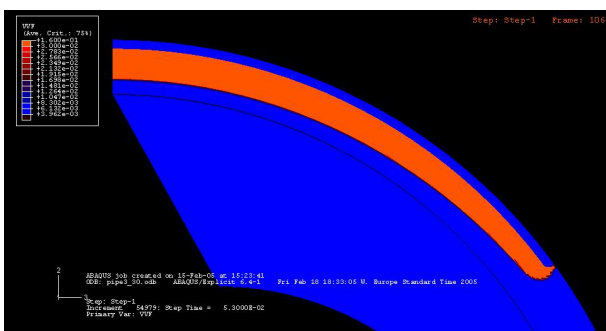

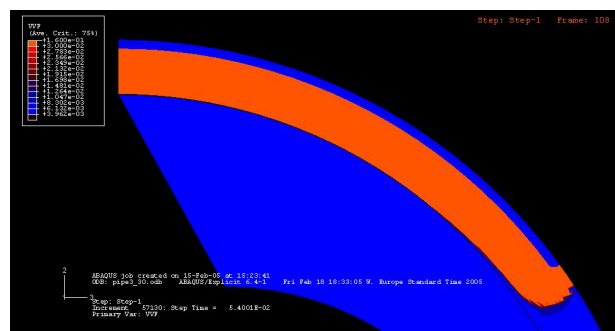Figure E.6: $\tau = 0.0525$ s

Figure E.7: $\tau = 0.0530$ s

Figure E.8: $\tau = 0.0540$ s

Affirmation

Hereby I confirm that I conducted this task without forbidden help of any third party and without using other sources than mentioned. Notions directly or indirectly taken out of external sources are identified as of that ilk.

Trondheim, March 2005   Lutz Zybell